Chlorophyll-a Variation Trends in Marginal Seas: Assessing the Impact of Global warming and Anthropogenic Activities Using Time Series Satellite Data (1998-2020)

Nan Yao[1], Xiaoyu Zhang[1,2*], Lei Bi[1], Shuchang Ma[1], Andrew B. Cundy[3], Haiyan Jin[4], Renyi Liu[1]

[1]School of Earth Sciences, Zhejiang University, Hangzhou, 310058, China
[2]Hainan Institute, Zhejiang University, Sanya, 572000, China
[3]GAU-Radioanalytical, School of Ocean and Earth Science, National Oceanography Centre (Southampton), University of Southampton, Southampton, UK, SO14 3ZH
[4]State Key Laboratory of Satellite Ocean Environment Dynamics, Second Institute of Oceanography, Ministry of Natural Resources, Baochubei Road 36, Hangzhou 310012, PR China

Correspondence to: X. Zhang (zhang_xiaoyu@zju.edu.cn)

Abstract. Global warming has been identified as the main cause of the decline of surface chlorophyll-a (Chl-a) concentrations in the oceans. Conversely, an increase in Chl-a concentration has been observed in a number of marginal seas over recent decades due to increasing anthropogenic input of key nutrients. However, with the intensification of global warming, its impact on Chl-a in coastal waters has been rarely studied, with the superimposed effects of human regulation of nutrients emissions. To fill this gap, this study provides a comparative analysis of enclosed versus open marginal seas, revealing divergent physiological and ecological responses to rising SST across different nutrient regimes. This study utilized time series of ocean color satellite data from 1998 to 2020 to examine the spatio-temporal distribution of Chl-a in a range of marginal seas, and its relationship with environmental factors, particularly with sea surface temperature (SST), photosynthetically active radiation (PAR) and surface wind speed (SWS) are considered as well. The results suggested that the sea areas examined with varying mixing and water exchange characteristics and degrees of human influence have differing responses (in terms of their Chl-a trends) to increasing SST. Specifically, in eutrophic closed seas with weak hydrodynamic exchange capacity, such as the the Bohai Sea, increasing SST did not apparently suppress Chl-a concentration, instead, a continuous increase in Chl-a was observed in the center of the sea. In comparison, the open marginal seas examined show strong negative relationships between SST and Chl-a with increasing distance offshore regardless of the degree of pressure from human activities, indicating that expected global warming effects driving reductions in Chl-a are extending to nearshore / marginal sea areas. This trend may be exacerbated due to stricter environment management policies imposed in recent years which have reduced anthropogenic nutrient inputs. Distinct from the above effect of global warming, PAR and SWS shape Chl-a in ways that are strongly modulated by geography and climate. PAR is the dominant positive control only in the Amazon estuary, where equatorial cloudiness and high turbidity create a light-limited regime, so any PAR increase directly stimulates phytoplankton. In mid-latitude open waters, PAR is secondary to SST: its seasonal rise is coupled to SST and therefore correlates negatively with

Chl-a once thermal stratification reduces nutrient supply. SWS emerges as a key driver in the three open regimes (the East China Sea >the Eastern Coast of the US> Amazon shelf), through injecting nutrient-rich cold deep water and episodically raising Chl-a. Inside the two enclosed seas (the Bohai Sea and the Gulf of Mexico), correlations with both PAR and SWS are weak ($|r| < 0.2$); Thus, PAR and SWS control Chl-a in a complex way, but both are more or less linked to SST and nutrients input. This study highlights the complex interaction between primary production, SST, nutrient inputs and hydrodynamic exchange, and environmental protection controls under the dual pressures of changes in human activity and coastal development, and global warming.

1 Introduction

Marine phytoplankton account for approximately half of the Earth's primary productivity and play a key role in ocean biogeochemical cycles and global climate processes (Field et al., 1998). As a biological carbon pump (BCP) marine phytoplankton accounts for about 26% of the global carbon sink (Dai et al., 2022; Friedlingstein et al., 2022; Jin et al., 2020; Letscher et al., 2023). Phytoplankton biomass is not only a key index for monitoring marine ecology and environment, but also provides an important basis for accurate estimation of oceanic primary productivity, carbon sinks, and food security.

Numerous studies have indicated that an observed decline of phytoplankton biomass over the past century in global oceans, can be attributed to increasing SST due to global warming (Baker and Geider, 2021; Behrenfeld et al., 2016; Boyce et al., 2010; IPCC, 2021). Since the beginning of the 20th century, a general rise in SST (specifically, an average temperature increase of 0.6 °C in the upper ocean) has led to the strengthening of water column stratification. This limits vertical nutrient exchange, resulting in reduced nutrient concentrations in upper waters, which in turn limits the growth of phytoplankton (Mizuta and Wikfors, 2020). It has been estimated that 80% of the observed decline in marine phytoplankton biomass from 1899 to 2008 is related to climate change, with the rate of Chl-a concentration reduction increasing with distance from coast (Boyce et al., 2010). In the Pacific and Atlantic oceans in particular, during 1998-2007, waters with low Chl-a concentration (Chl-a ≤ 0.07 mg/m3) expanded at an annual rate of 0.8 % – 4.3 % , replacing about 800,000 square kilometres of water with high Chl-a concentration each year (Gregg et al., 2005; Gregg and Rousseaux, 2014). Additionally, as one of the most prominent sources of interannual natural variability in the Earth's climate system, global warming may alter the frequency and intensity of El Niño-Southern Oscillation (ENSO) events, thereby inducing extensive positive or negative SST anomalies across the Pacific and beyond. This introduces additional complexity in deciphering the SST-Chl-a concentration relationship at regional and interannual scales (Cai et al., 2022; Hou et al., 2024).

In contrast, near-shore phytoplankton biomass shows a long-term increase, despite the global rise in SST, which is believed to be due to anthropogenic eutrophication (Boyce et al., 2010; Jickells, 1998; Kong et al., 2019; Lee et al., 2019; Marrari et al., 2016). Regional studies present conflicting conclusions regarding the relationship between SST and Chl-a in coastal waters, which may be due to a number of different regional oceanographic and anthropogenic effects. Coastal regions with upwelling, such as the Eastern North Atlantic (Siemer et al., 2021) and Bay of Bengal (Chowdhury et al., 2021), exhibit a negative correlation between Chl-a and SST and seasonally dependent. Here, notwithstanding nutrient inputs from land, upwelling plays a crucial role in transporting colder deeper water with abundant nutrients to the sea surface, stimulating local phytoplankton population and resulting in the negative correlation between SST and Chl-a (e. g., Chen et al., 2021; Favareto et al., 2023). However, this natural physical control can be masked or even reversed in coastal systems where anthropogenic pressures dominate. In other areas, nutrient run-off and other anthropogenic activities have generated strong increases in primary productivity from the mid-20th century, despite SST increases. For example, in the Baltic Sea, an increase in cultural eutrophication since the 1950s has produced marked sedimentary changes in a range of organic geochemical indicators. These indicators, including those reflecting increased phytoplankton biomass, have been suggested as important secondary markers for the proposed Anthropocene epoch at this candidate Global Boundary Stratotype Section and Point (GSSP) site (Kaiser et al., 2023). Other anthropogenically enhanced processes have also profoundly altered the correlation between Chl-a and SST. These include predation pressure—particularly in aquaculture areas, where filter-feeding organisms reduce phytoplankton biomass (e.g., Frau et al., 2021; Mao et al., 2020), and commercial fishing, which indirectly affects phytoplankton biomass by altering zooplankton and fish abundance (Campos-Silva et al., 2021; Reid et al., 2000).

In addition, the complex responses of photosynthetically active radiation (PAR) and surface wind speed (SWS) to global warming exert additional controls on upper-layer Chl-a, making it difficult to clarify the sole impact of warming independent of these concurrent physical changes. Photophysiological processes—namely photoinhibition under supersaturating irradiance and photoadaptation through adjustments in pigment composition, light-harvesting complex abundance, and non-photochemical quenching capacity, exert first-order control on upper-ocean Chl-a inventories (Moradi and Moradi, 2020; Pi et al., 2019). However, despite large previous efforts there are still significant gaps in the current understanding of the variability of Chl-a and its relation to the PAR on regional seasonal time scales. The influence of SWS on Chl-a is non-linear and spatially heterogeneous (Liu et al., 2026; Wang et al., 2025; Zhang et al., 2022). Generally, moderate SWS intensifies coastal upwelling, injecting nutrient-rich deep water into the euphotic zone and stimulating phytoplankton growth. Whereas excessive wind forcing deepens the mixed layer and shortens residence time, impeding phytoplankton retention in the illuminated layer and ultimately suppressing biomass accumulation. Moreover, the magnitude and even the sign of this relationship vary with regional circulation and seasonal stratification (Wang and Xiu, 2022).

To better understand the controls on temporal and spatial Chl-a concentration trends in coastal waters, this study assesses the relationship between Chl-a concentrations (a proxy for phytoplankton biomass) and SST in five coastal waters with varying levels of anthropogenic activity, using time series satellite data from 1998 to 2020. Indices including PAR and SWS are also incorporated to comprehensively explore the underlying mechanisms driving the evolution of Chl-a. Specifically, we examine two enclosed bays with high levels of human interference (the Gulf of Mexico in the United States and the Bohai Sea in China), and three open sea areas with varying degrees of human interference (the Amazon Estuary, The eastern coastal waters of the US, and the Changjiang Estuary). The objective is to elucidate the distinct responses of phytoplankton to sustained global warming in the presence of anthropogenic nutrient inputs and to distinguish the ecological effects of warm water intrusion from those of human activities.

The remainder of this paper is structured as follows. Data and Methods describe the study areas, satellite data sources, and the methodologies employed, including trend analysis, stability assessment, and correlation analysis. Results presents the spatio-temporal distribution characteristics of Chl-a, its historical variation trends, stability, and its relationship with key environmental factors across the five marginal seas. Based on these findings, Discussion provides a comprehensive analysis of the mechanisms driving Chl-a variations, focusing on the roles of natural environmental factors, global warming, and anthropogenic nutrient inputs. Finally, Conclusions summarizes the main findings of the study and discusses their ecological implications under the dual pressures of global warming and human activity.

2 Data and Methods

2.1 Study areas

This study focused on five Marginal Seas over the world with different water exchange rate and anthropogenic activities (shown in Fig. 1) (Cui et al., 2021; Dobson et al., 2000; Lloyd et al., 2019). The enclosed seas (here, the Bohai Sea and the Gulf of Mexico) are usually characterized by very slow water exchange, which limits the diffusion and transportation of land sourced pollutants and produces a limited self-purification capability. The three open sea areas studied were the Changjiang Estuary, the Eastern Coastal Waters of the US and Amazon Estuary. An open sea area is defined in this study relative to the enclosed sea area, that is, a near shore area with only one land boundary. Generally, the hydrodynamic conditions in open sea areas are favourable for the diffusion of land-derived materials.

The East China Sea is one of the biggest marginal seas of the northwestern Pacific with complex circulation systems (Fig. 1a). The Tsushima and Kuroshio currents with high temperature and salinity prevail in the eastern side of the East China Sea. On the western side, the Zhemin Coastal Currents, formed by the Changjiang River Plume with the intrusion of the Taiwan Warm Current, dominate. However, due to increasing human activities in the Changjiang River Basin, there has been a significant increase in nutrient inputs, leading to more frequent occurrences of harmful algal blooms (HABs) (Ministry of Ecology and Environment, PRC, 2001, 2021; Zhou et al., 2022).

The Eastern Coastal Waters of the US, located to the northeast of the Gulf of Mexico, are strongly influenced by the Gulf Stream, resulting in enhanced primary productivity (Ma and Smith, 2022). Numerous rivers including the Hudson River, Delaware River, Susquehanna River, Joptank River, and others, flowing through highly urbanized cities, discharge pollutants and have increased the frequency of HAB events in the past decades (e.g., Mizuta & Wikfors, 2020).

In Amazon Estuary, the tropical Atlantic surface circulation, specifically the North Brazil Current running northwestward along the Brazilian coastline, exerts a dominant influence over the area (Fig. 1c). The Guyana Current is also active in this sea area. HABs in Amazon Estuary typically occur during the spring and summer, as they are influenced by the seasonal flow variations of the Amazon River. Notably, there has been an increase in HAB events since 2008 (e.g., Dai et al., 2023; Hallegraeff et al., 2021; Subramaniam et al., 2008).

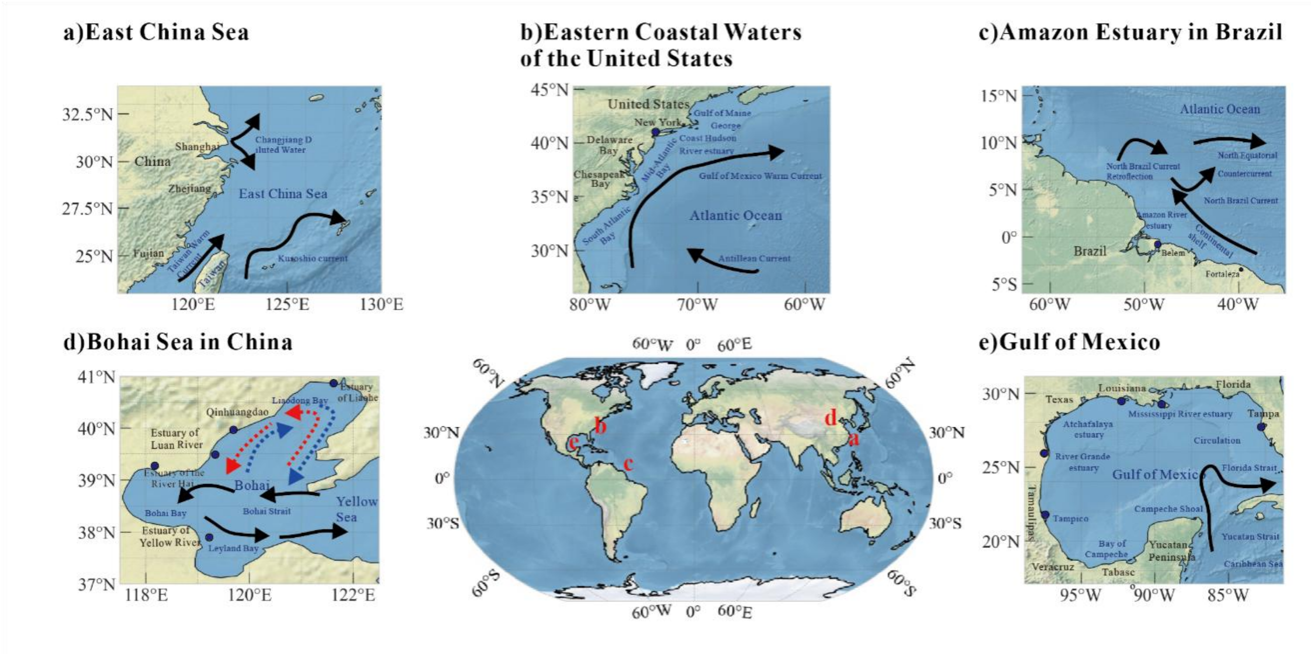

Figure 1. The geographical locations and major current systems of the five studied sea areas. a) the East China Sea located in the range of 117 °E~131 °E and 23 °N~33°N; b) the eastern coastal waters of the US located in the range of 81.6°W – 57.66° W and 27.5°N – 43.3°N; c) Amazon Estuary located in the range of 16°N – 6°S and 61°W – 37°W; d) the Bohai Sea located in the range of 37° N– 41°N and 117° E– 123°E; e) the Gulf of Mexico located in the range of 17.09°N – 31.16°N and 98.86°W – 81.28°W. Note: The base maps for the land and ocean portions of the map artifacts are land cover data, and the ocean polygon data (rendered in grey), and are available for download from Natural Earth (https://www.naturalearthdata.com/).

The Bohai Sea is undergoing severe anthropogenic disturbance with coastal runoff from at least 40 rivers, such as the Yellow River, Haihe River, Liaohe River, and so on. The influx of significant amounts of pollutants, including sewage, has severely disrupted the local aquatic ecology (Ministry of Ecology and Environment, PRC, 2021). The circulation of the Bohai Sea exhibits seasonal variations (Fig. 1 d), significantly impacting the transport of pollutants (Wu et al., 2023; Zhang et al., 2022). The rate of seawater exchange with the Yellow Sea strongly influences the ecological environment within the Bohai Sea (Ju et al., 2020).

The circulation system in the southeast of the Gulf of Mexico (Fig. 1f) acts as the primary hydrodynamic force, stimulating the local primary productivity (Damien et al., 2021). Whereas, the northern part of the Gulf of Mexico is significantly influenced by nutrient inputs originating from the Mississippi-Atchafalaya Basin. The accelerated growth of industry and extensive use of fertilizers have led to excessive production of algae (e.g., Fu et al., 2020; Yingling et al., 2022) .

Table 1. Comparative environmental and demographic overview of study regions

Sea area	Attribute of the sea area	Hydrodynamic exchange capability	Population density of the basin (population/km²)	Eutrophic state	Human regulation
The East China Sea	Open	High	563.88	High	Very High
The eastern coastal waters of the US	Open	High	151.28	Moderate to High	High
Amazon Estuary	Open	High	36.91	Low	Low
The Bohai Sea	Enclosed	Moderate	344.78	High	Very High
The Gulf of Mexico	Enclosed	High	71.61	Moderate to High	High

The five selected sea areas cover varying degrees of human activity and hydrodynamic exchange capability, as summarized in Tab. 1. Population density data for the surrounding basins were obtained from the LandScan (2020) high-resolution global population dataset (Lebakula et al., 2025) and were used here as a proxy for anthropogenic pressure. The term "Human regulation" in this context quantifies the intensity of human activities within the basin that regulate nutrient inputs and environmental stress on the marine ecosystem.

2.2 Data Sources

Concerning the influence by various chemical, hydrological, meteorological and biological factors (e.g., Hong et al., 2023; ; Martinez et al., 2020; Xi et al., 2021), the satellite derived datasets of Chl-a, combined with SST, PAR, and SWS, were used to discuss temporal and spatial variation trends and interactions. Meanwhile, SST were also used to identify periods of which the seawater was heated. PAR and SWS were included as key environmental indices known to influence phytoplankton growth and distribution. PAR directly constrains photosynthesis, while SWS affects vertical mixing, nutrient entrainment from deeper layers, and light availability by modulating the mixed layer depth. Tab. 2 shows data types, data sources, temporal and spatial resolution, spanning periods, and download websites used in this study.

These datasets, derived through algorithmic processing of raw satellite imagery, were recognized for their reliability and comprehensive temporal coverage, making them particularly valuable for studying waters with complex optical properties, such as coastal and estuarine environments (Pisano et al., 2016; Zhang et al., 2006). We applied a consistent preprocessing method (see Section 2.3) to establish a unified satellite dataset from multiple satellites. Taking Chl-a and PAR as example: before constructing the time series dataset, however, the satellite Chl-a and PAR data were divided into three periods according to availability of different satellite products. (T1 period: Jan 1998-Dec 2002, Chl-a and PAR products only from SeaWiFS are available; T2 period: Jan 2003-Dec 2010, overlap period, Chl-a and PAR products from both MODIS and SeaWiFS are available; T3 period: Jan 2011-Dec 2020, Chl-a and PAR products are available only from MODIS). The two satellite sensors (SeaWiFS and MODIS) have different operational periods, so systematic errors was eliminated before merging them into a long-term data set. See Appendix A for an in-depth explanation of the data preprocessing methodology. The SST data, critical for the study, were extracted from the AVHRR Pathfinder dataset (Pisano et al., 2016). Additionally, SWS data were incorporated from the CCMP Wind Vector Analysis Product (Mears et al., 2019).

Table 2. Monthly satellite derived datasets used in this study

Data type	Data sources	Temporal/spatial resolution	Periods	Links	Last accessed date
Chl-a	SeaWiFS L3 Product	Monthly/9.28 km	1998.1~2010.12	https://oceancolor.gsfc.nasa.gov/l3/order/	25-May-26
	Aqua-MODIS L3 Product	Monthly/4.64 km	2008.1~2020.12	https://oceancolor.gsfc.nasa.gov/l3/order/	25-May-26
PAR	SeaWiFS L3 Product	Monthly/9.28 km	1998.1~2010.12	https://oceancolor.gsfc.nasa.gov/l3/order/	25-May-26
	Aqua-MODIS L3 Product	Monthly/4.64 km	2008.1~2020.12	https://oceancolor.gsfc.nasa.gov/l3/order/	25-May-26
SST	AVHRR Pathfinder SST	Monthly/0.25 deg	1998.1~2020.12	https://www.ncei.noaa.gov/products/avhrr-pathfinder-sst	25-May-26
SWS	CCMP Wind Vector Analysis Product	Monthly/0.25 deg	1998.1~2020.12	https://www.remss.com/measurements/ccmp/	25-May-26
Ocean boundary	Natural Earth Ocean	-/110m	-	https://www.naturalearthdata.com/downloads/110m-physical-vectors/110m-ocean/	25-May-26

2.3 Methods

Fig. 2 shows a flowchart of this study. To harmonize datasets with different spatial resolutions, all raster datasets were reprojected and resampled to a common reference grid before further analysis. A MODIS grid file covering the study areas was used as the spatial reference, and Chl-a, PAR, SST, and SWS datasets were resampled using bilinear interpolation through the GDAL Warp function. This procedure ensured that all variables had consistent projection, pixel size, and spatial extent. The temporally matched monthly datasets were then used for subsequent analyses. To the availability of satellite datasets of Chl-a, PAR, SWS, and SST (from 1998 to 2020), the correlation and interaction between Chl-a changes and seawater warming was sorted out following the steps below: (1) the temporal trends of seasonal and annual Chl-a in the five different study areas were analyzed using the Mann-Kendall (M-K) Trend Analysis method. (2) the Chl-a stability and variation coefficients of each pixel were calculated to evaluate the varying degree of Chl-a spatially, correlation analyses, and PCA (principal component analyses) were conducted to determine the main marine environmental factors impacting Chl-a in each sea area. (3) the global warming periods are identified with SST dataset. (4) image-by-image metric correlations between Chl-a and anthropogenic SST rising were calculated for specific time periods of interest.

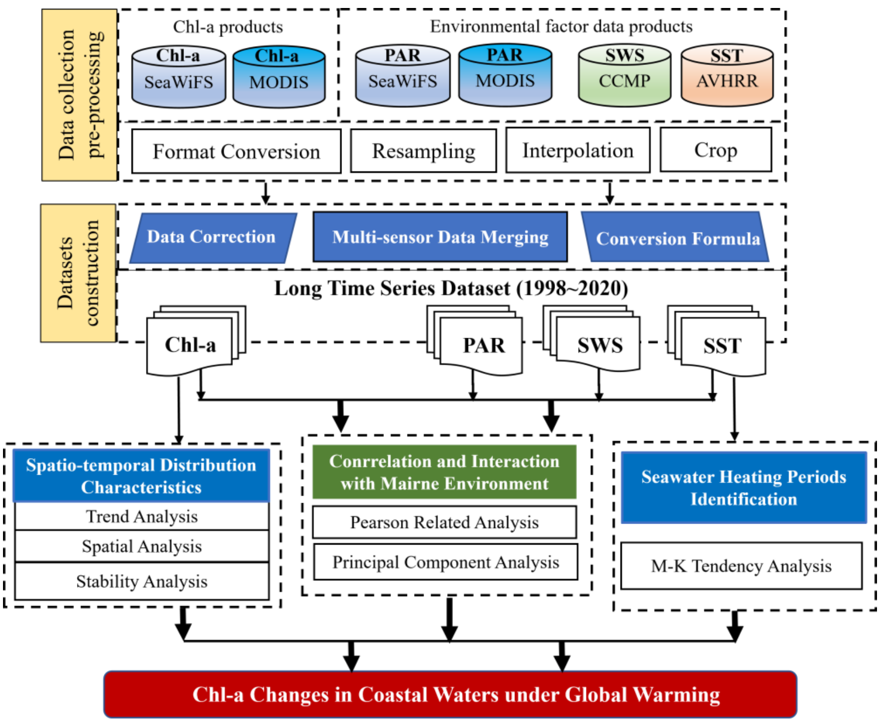

Figure 2. Flowchart for assessing the impact of global warming and anthropogenic activities on Chl-a trends using time-series satellite data

2.3.1 Time Series Analysis

The least squares method, widely used in time series analyses related to climate change (Mudelsee, 2019), was applied to obtain trends in Chl-a concentration over the period 1998-2020. The time series for trend analysis was composed of Chl-a values for each pixel in the study area, with outliers removed if they exceeded three times the standard deviation from the mean. See Appendix B for details of calculation. The results obtained are used to assess the local Chl-a response to global warming.

The M-K Trend Analysis method is a non-parametric statistical approach widely employed to discern temporal trends in time series data (e.g., Wang et al., 2021). This method assesses whether there is a statistically significant increasing or decreasing trend by comparing the relative ranks of data points over time. The test statistic UF (Upward Factor) is calculated to identify the sequence of potential upward trends, while UB (Downward Factor) is derived from the reversed data series to pinpoint the timing of potential trend shifts. The formulas for UF and UB are as follows:

$$\mathrm{UF}_k = \frac{s_k - E(s_k)}{\sqrt{\mathrm{Var}(s_k)}}, (k = 1,2,\ldots,n) \quad (2\text{-}4)$$

$$\mathrm{UB}_k = \frac{E(s_k) - s_k}{\sqrt{\mathrm{Var}\ (s_k)}}, (k = 1,2,\ldots,n) \quad (2\text{-}5)$$

of which s_k is a statistical measure defined in the Mann-Kendall test; $\mathrm{Var}\ (s_k)$ represents the variance of the calculated statistical measure; $E(s_k)$ represents the expected value of the statistical measure. The relevant calculation formulas are provided in Appendix C.

In the M-K test, the null hypothesis of no trend is rejected at the 5% significance level if the absolute value of UF exceeds 1.96. A positive UF value indicates an upward trend, while a negative value indicates a downward trend. The intersection point of the UF and UB curves, if it occurs within the confidence limits, suggests the year of a potential abrupt change in the trend. The detailed discrimination criteria for trend significance and direction are summarized in Tab.3.

Table 3. Discrimination criteria for M-K test

Threshold	$\alpha < 0.05$ $(-1.96 \le \mathrm{UF} \le 1.96)$	$\alpha \ge 0.05$ $(\mathrm{UF} > 1.96 \ \| \ \mathrm{UF} < -1.96)$
$\mathrm{UF} > 0$	Increasing but not significant	Significantly increasing
$\mathrm{UF} < 0$	Decreasing but not significant	Significantly decreasing

where α is the level of confidence.

2.3.2 Spatio-temporal trends analysis

The slope analysis method (Wang, 2006) was employed to analyse the spatio-temporal trends of Chl-a in five different locations. From 1998 to 2020, the annual variation rate of Chl-a was calculated with the least squares method using time-series data from each pixel within the study region. A slope>0 indicates an upward trend of Chl-a at the corresponding pixel, and vice versa. The larger the value, the faster the increase, see Appendix C for details.

The stability of Chl-a was calculated by computing the Coefficient of Variation (CV) of Chl-a time-series data for each pixel, Chl-a stability was classified into five levels based on CV values: "High Stability" (CV < 0.05) indicates minimal variability; "Medium to High Stability" (0.05 ≤ CV < 0.10) reflects minor fluctuations; "Medium Stability" (0.10 ≤ CV < 0.15) shows moderate variability; "Medium to Low Stability" (0.15 ≤ CV < 0.20) represents significant fluctuations; and "Low Stability" (CV ≥ 0.20) signifies highly unstable conditions, see Appendix D for details.

2.3.3 Seawater Heating Period Identification

The warming periods were identified based on SST changes during 1998-2020 in the five locations using a four-year moving time window (Fig. 3). This window length was chosen to capture sustained, low-frequency warming signals indicative of climate-scale changes, while smoothing out shorter-term interannual variability (e.g., linked to seasonal cycles or transient weather events). Periods exhibiting the most pronounced SST rise within these 4-year windows were selected for analysing the interaction between Chl-a and SST increase. For comparison, periods of relatively stable SST were identified using the same 4-year window methodology.

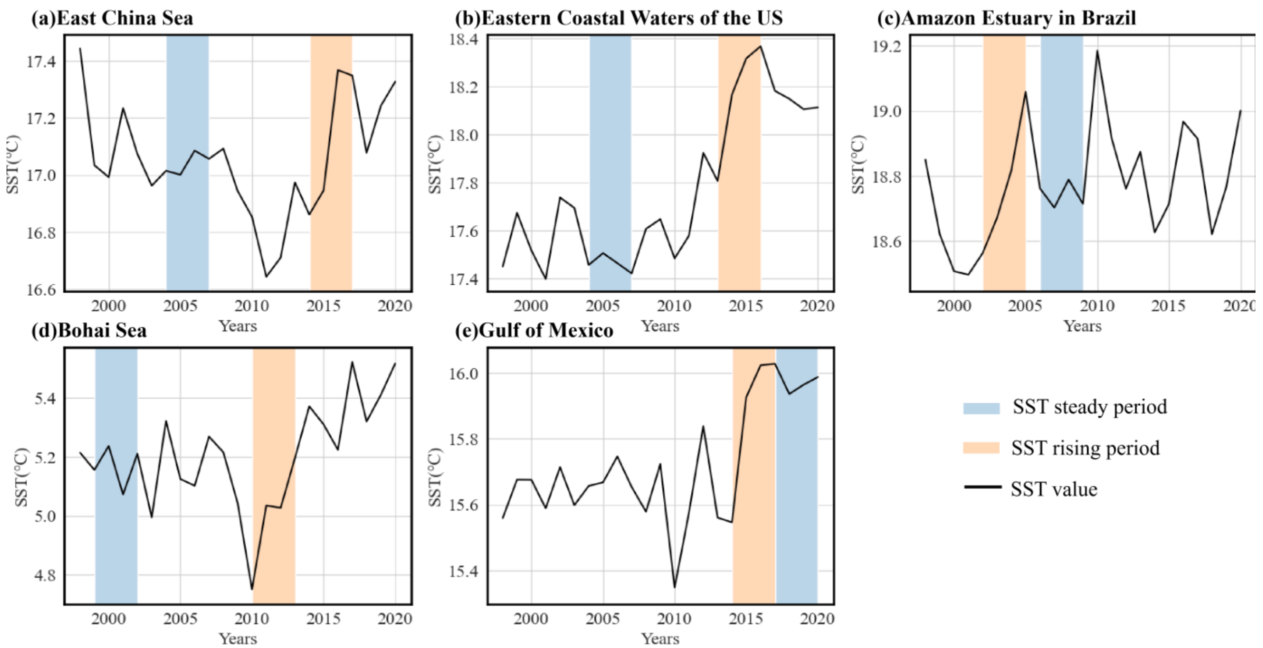

Figure 3. The variation of SST of the five locations from 1998 to 2020, and identified periods of SST rise and periods of SST stability.

Two time windows identified with the largest SST rise and the most stable SST in the five locations are shown in Tab. 4. The largest SST rising periods exhibit significant variation rates, reaching up to 0.120–0.200℃/yr. In contrast, the most stable SST periods correspond to variations of approximately 0.005–0.010℃/yr. The main SST rising periods of the Gulf of Mexico, the East China Sea and the eastern coastal waters of the US tally with the time windows of the most intense El Niño event recorded (2014-2016), whereas distinct rises in SST for Amazon Estuary and Bohai Sea are coincident with the occurrence of the El Niño windows of 2002-2003 and 2009-2010, respectively (Cai et al., 2021; https://www.cpc.ncep.noaa.gov/products/analysis_monitoring/ensostuff/ONI_v5.php).

Table 4. Periods identified with different SST variation trend

Sea area type	Sea area	SST steady period /year	SST rising period		
			Period/year	SST rising (°C)	SST rising rate (°C/yr)
Open sea area	The East China Sea	2004~2007	2014~2017	0.488	0.189
	The eastern coastal waters of the US	2004~2007	2013~2016	0.561	0.183
	Amazon Estuary	2006~2009	2002~2005	0.495	0.163
Enclosed sea area	The Bohai Sea	1999~2002	2010~2013	0.445	0.133
	The Gulf of Mexico	2017~2020	2014~2017	0.482	0.154

2.3.4 Correlation Analysis

We performed Pearson correlation and PCA to identify the impacts on the Chl-a concentrations from environmental factors for each study area. Specially, to understand how global warming affects phytoplankton in coastal sea waters, quantitative determination of the correlation between Chl-a concentrations and SST for each pixel within the study area were performed in SST stable period and in SST rising period respectively (Maćkiewicz and Ratajczak, 1993). For PCA, monthly raster data of Chl-a, SST, PAR, and SWS were first spatially averaged over valid pixels within each study area to obtain regional monthly mean series, which were then normalized using min-max normalization. The PCA was conducted on these normalized regional time series to identify the dominant environmental gradients associated with Chl-a variability. In detail, the time series data for annual mean Chl-a and SST were normalized to address their inherent non-normal distribution. Through comparing the changes in correlations between Chl-a and SST across different sites, under conditions of thermal variation and stability, and considering the local hydrological characteristics, we delved into the mechanisms by which global warming influences Chl-a.

3 Results

3.1 Spatial distribution characteristics of Chl-a

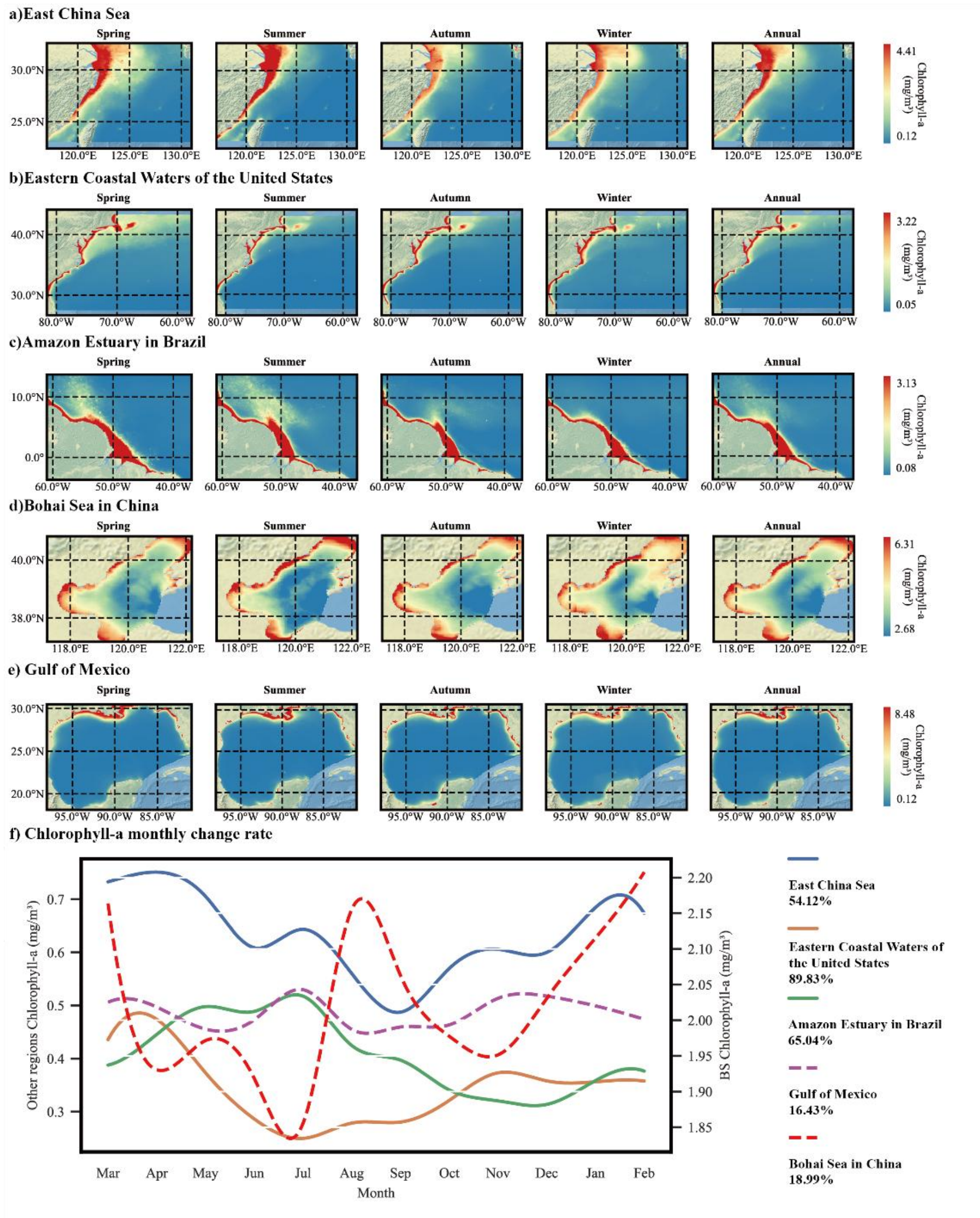

Figure 4. Spatial distribution of annual and seasonal Chl-a at the five sites. a)- e) represents the East China Sea, the Eastern Coastal Waters of the United States, Amazon Estuary, the Bohai Sea, and the Gulf of Mexico respectively. f) presents the monthly variation of Chl-a concentrations in these regions, of which the Bohai Sea utilizes the right y-axis, while the other four seas use the left y-axis. The data in the right is the monthly change rate. Areas shown in light grey blue (■) have no available data.

Fig. 4 shows the seasonal and annual spatial distribution of Chl-a concentrations for the five study areas. All locations show distinct decreasing Chl-a with distance offshore, and higher values are mainly found in estuaries and bays. Particularly, areas with higher Chl-a are more uniformly distributed in the Bohai Sea with limited water exchange, while the Gulf of Mexico shows similar spatial distribution tendency to those open sea areas due to strong water exchange with the Atlantic.

From highest to lowest, Chl-a concentration varies in the order the Bohai Sea > the East China Sea> the Gulf of Mexico> the eastern coastal waters of the US≈ Amazon Estuary. As a severely eutrophic enclosed sea area, the Bohai Sea maintains high values between 1.6 and 2.5 mg/m^3 throughout the year. Meanwhile the East China Sea, which is an open sea in highly eutrophic state, exhibits a consistently higher annual Chl-a, with spring values frequently exceeding 0.6 mg/m^3. The other three regions all have year-round Chl-a below 0.6 mg/m^3.Chl-a concentrations in the open sea area exhibit greater susceptibility to seasonal variations than those in enclosed seas with restricted exchange as show in Fig. 4f, with change of the monthly average rate of Chl-a concentration surpassing 50%.

3.2 Historical Chl-a variation in study regions

The Mann-Kendall trend test reveals distinct temporal trends in Chl-a concentrations across the five study regions (Fig. 5). Specially, a statistically significant overall increasing trend is suggested in annual and all seasonal Chl-a concentrations in the Gulf of Mexico ($p < 0.05$). While a slightly increase tendency of Chl-a is observed in the Eastern Coastal Waters of the US with a rate of 0.0301 $mg/m^3 \cdot a$, no statistically significant trends ($p > 0.05$) are observed in the East China Sea, U.S. East Coast, Amazon Estuary, or the Bohai Sea. However, distinct continuous increase of Chl-a is indicated in summer in sea area of the Eastern Coastal Water of the US.

Notably, both the Bohai Sea and the East China Sea exhibit a two-stage change, with decreasing tendency after a continuous increasing, although the decline of the East China Sea is insignificant. The turn point of the Bohai Sea occurred in 2013, earlier than the East China Sea in year 2017.

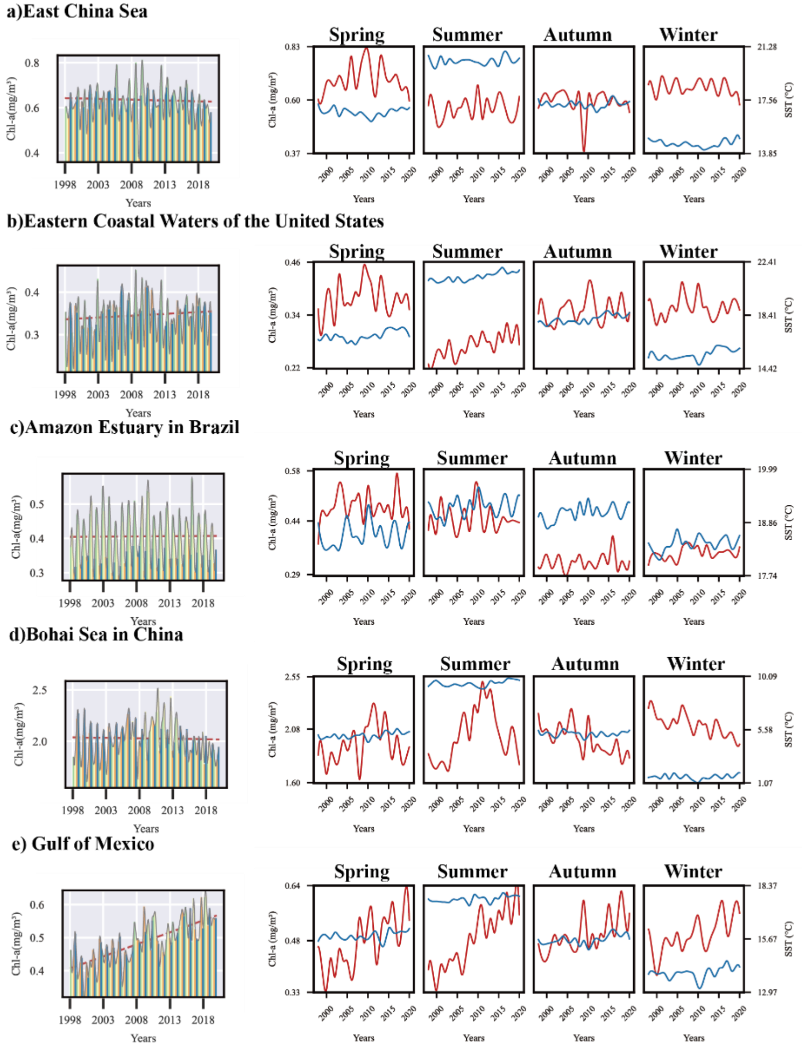

Figure 5. Historical Chl-a annual and seasonal variation for the five study locations from 1998 to 2020. a)- e) represents the East China Sea, the Eastern Coastal Waters of the US, Amazon Estuary, and the Gulf of Mexico respectively. The red dash line in the first bar graphs represents regressive trend line. The red and blue curve line in line graphs represent the variation of seasonal Chl-a and SST respectively.

The seasonal mean Chl-a concentrations do not always follow the same temporal trend as the annual mean. However, in the Gulf of Mexico, all four seasonal means show consistent increasing trends that align with the annual mean trend (Fig. 5). The correlation analysis between annual and seasonal Chl-a (Tab.5) suggested that the temporal change of annual Chl-a in the Bohai Sea are controlled dominantly by the spring and summer Chl-a, whereas in the Gulf of Mexico, the annual trend is more uniformly correlated across all seasons due to its different hydrodynamic regime. In open sea areas, winter and spring Chl-a concentrations are strongly correlated with the annual mean and thus serve as the primary drivers of the annual trend. Amazon Estuary represents an exception, where summer and winter Chl-a are more important in determine the annual trend.

Table 5. Correlation analysis between seasonal and annual Chl-a Concentration

Open Sea Area			Enclosed Sea Area		
Sea Area	Season	Correlation coefficient	Sea Area	Season	Correlation coefficient
The East China Sea	Spring	0.638	The Bohai Sea	Spring	0.844
	Summer	0.454		Summer	0.780
	Fall	0.382		Fall	0.284
	Winter	0.496		Winter	0.427
The Eastern Coastal Waters of the US	Spring	0.711	The Gulf of Mexico	Spring	0.949
	Summer	0.576		Summer	0.926
	Fall	0.543		Fall	0.651
	Winter	0.618		Winter	0.905
Amazon Estuary	Spring	0.735			
	Summer	0.699			
	Fall	0.215			
	Winter	0.637			

3.3 Spatio-temporal variation of Chl-a

Fig. 6 and Appendix E illustrate the spatio-temporal variation rates of Chl-a from 1998 to 2020. Overall, coastal regions exhibit increasing Chl-a trends, whereas offshore areas show declining trends, with the exception of the Bohai Sea (Fig. 6d). The Bohai Sea has the largest area with positive annual growth (33.79%), while the Eastern Coastal Water of the US has the smallest (6.53%). Seasonally, the Bohai Sea also exhibits the most extensive Chl-a increase in summer (Fig. 6d), contrasting sharply with the U.S. East Coast, which shows the smallest growth area in summer (8.06%, Fig. 6b).

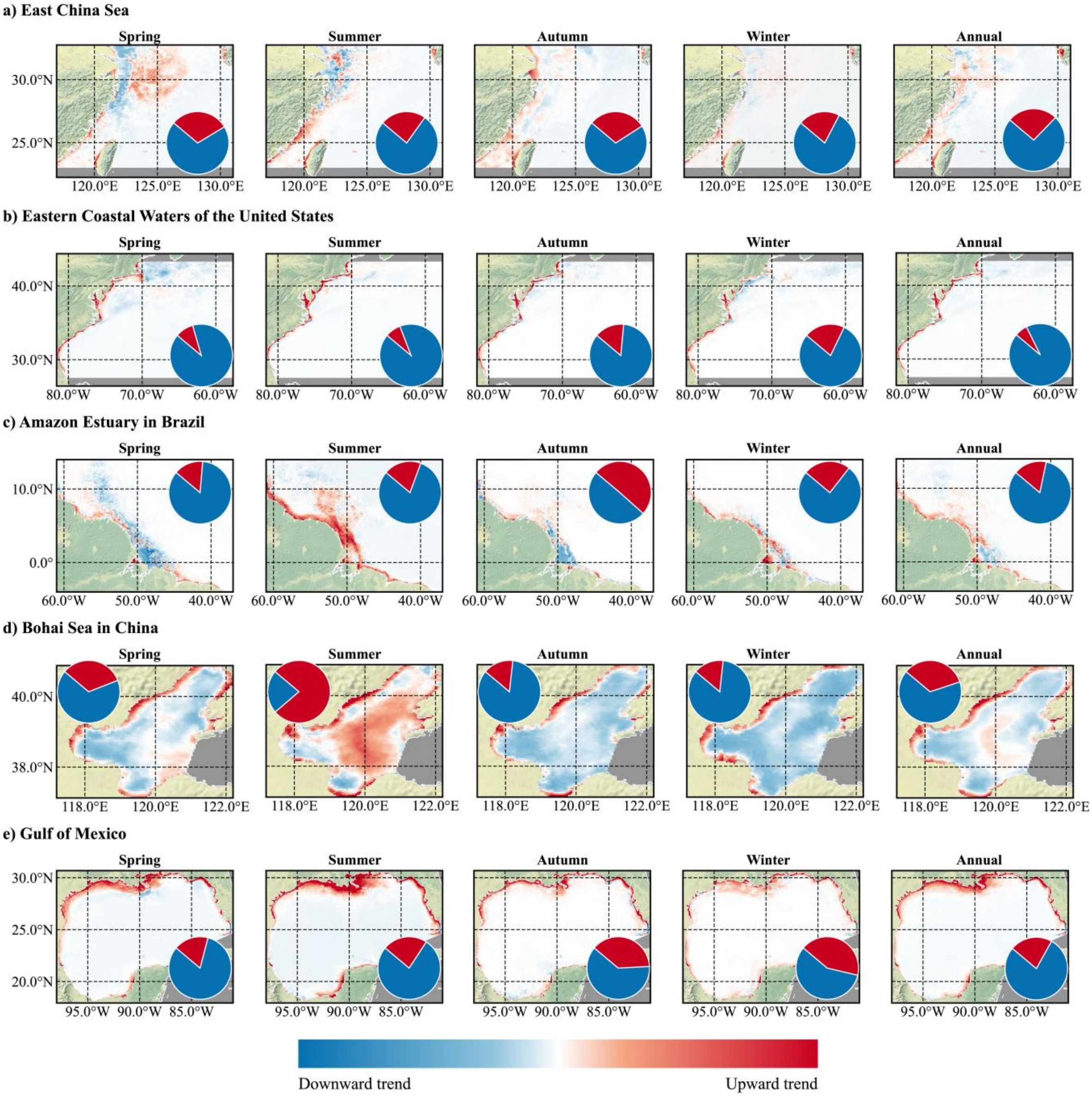

Figure 6. Temporal trend of seasonal and annual Chl-a in each pixel in the five locations. a)- e) represents the East China Sea, the Eastern Coastal Waters of the US, Amazon Estuary, and the Gulf of Mexico respectively. The pie chart shows the proportion of areas with downward (blue) and upward (red) tendency. Areas shown in slight grey blue have no available data.

However, a general decline in Chl-a levels is revealed across most time frames in the context of the Bohai Sea except in the central basin of the Bohai Sea in summer, where Chl-a concentrations have exhibited a sustained increase trend (Fig. 5d, 6d). This anomaly is likely the ecological lag effect of nutrient aggregation in the central basin, facilitated by the internal hydrodynamical patterns and weak exchange capability with outer oceanic currents. Such nutrient enrichment in the central basin, especially under the conditions of elevated summer temperatures, promoting algal blooms even amid reduced land-based inputs.

This dynamic, however, is intricately linked to the specific dimensions of the enclosed sea area and the intensity of human activities within. The Gulf of Mexico, an analogous enclosed marine ecosystem, does not exhibit comparable patterns in fluctuations of Chl-a concentrations. Strong influences from the Gulf Stream and Cuban Current enhance water exchange with the Atlantic, making its Chl-a patterns more akin to those of open seas. In contrast, in open seas, increasing Chl-a is primarily confined to coastlines and river plumes, such as the Changjiang Estuary in spring (Fig. 6a) and the Amazon Plume in summer (Fig. 6c).

3.4 Stability of Chl-a

The stability of Chl-a quantified by the coefficient of variation from 1998 to 2020 across five study regions is illustrated in Appendix F and Figure 7. Regions with obvious increasing or decreasing Chl-a trends possess lower stability. Overall stability varies by sea type: the open seas are less stable than the enclosed seas, and the East China Sea has the lowest stability among all studied waters.

Open seas include the East China Sea, the Eastern Coastal Waters of the US and Amazon Estuary. All of open seas present unstable Chl-a conditions in spring and summer. Pronounced seasonal discrepancies in Chl-a stability are widely detected in open ocean zones, as displayed in Figure 7a, 7b and 7c. Chl-a maintains higher stability in winter across all sea areas. Low stability is found in the Taiwan Strait, Gulf Stream and Amazon Plume, while relatively steady Chl-a status exists all year round in partial waters of the Changjiang Estuary and area near the mouth of Amazon River.

Enclosed seas show distinct stability patterns, represented by the Bohai Sea and the Gulf of Mexico. The Bohai Sea generally maintains moderate to high Chl-a stability, excluding coastal and estuarine areas. Its stability remains relatively high despite seasonal fluctuations, differing from the seasonal instability seen in open sea counterparts. By comparison, over 90% of the Gulf of Mexico features low or moderately low stability. Areas with intense human activities such as the northern Gulf and waters around the Florida Peninsula sustain poor stability throughout the year. Only the central Gulf was witnessed slightly improved stability in winter, attributed to the diminished human interference and decreased SST (Durán-García et al., 2017). Collectively, hydrodynamic conditions and anthropogenic disturbances jointly regulate Chl-a stability in both open and enclosed marine environments.

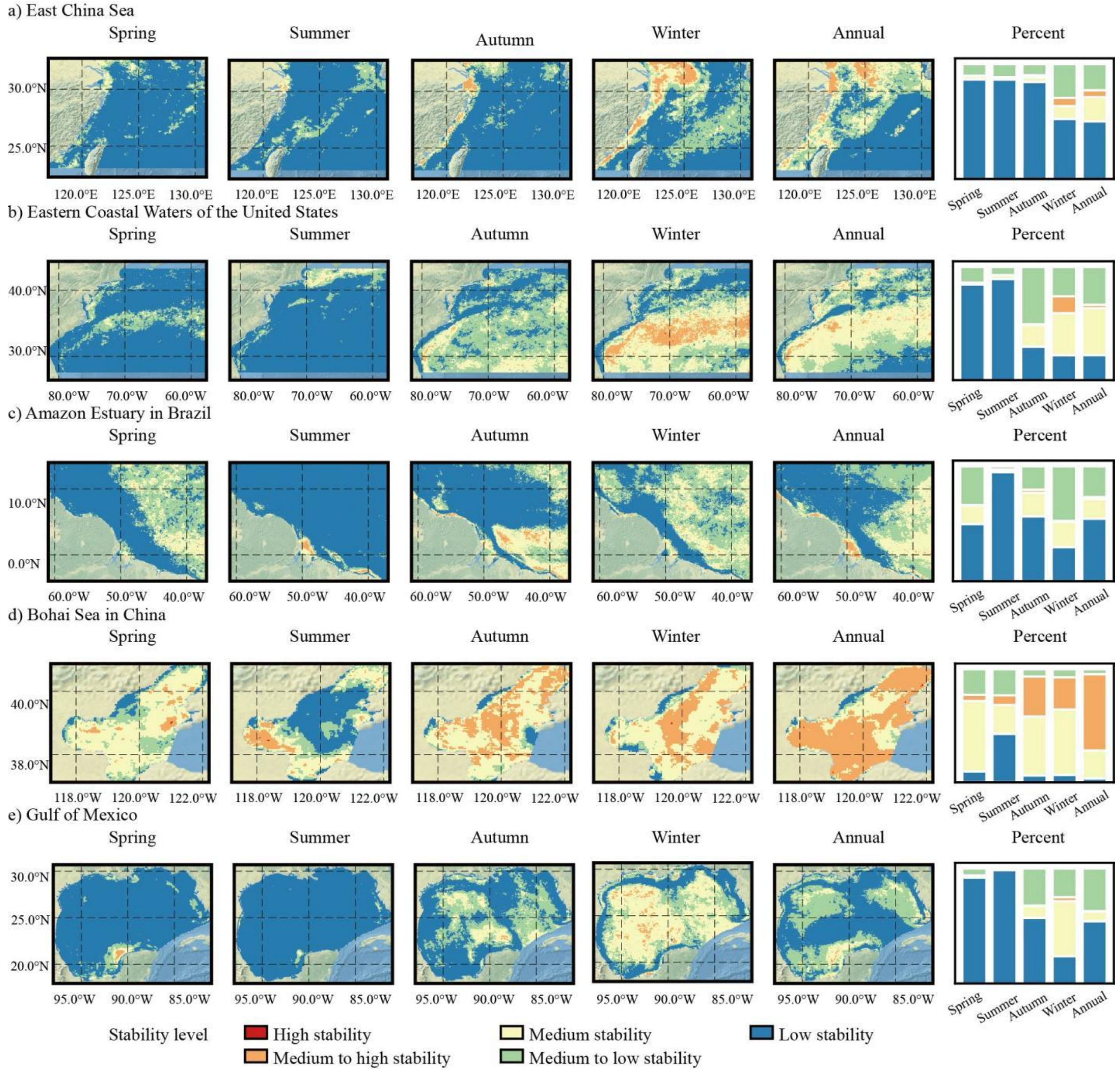

350 **Figure 7. The spatial distribution of the variation coefficient of seasonal and annual Chl-a from 1998 to 2020. a)- e) represent the East China Sea, the Eastern Coastal Waters of the US, Amazon Estuary, and the Gulf of Mexico respectively. The percentage bar chart shows the proportion of areas with different stability in each season.**

4 Discussion

4.1 Factors impacting spatio-temporal changes in Chl-a

To identify major environmental factors impacting the observed spatio-temporal changes in Chl-a in the five different locations, the three main environmental indices SST, PAR, and SWS were correlated and evaluated with Chl-a via Pearson correlation analysis and principal component analysis, details see section 2.3.4. Overall, the correlations between Chl-a and the various marine environmental indices vary significantly depending on study area as presented in Fig. 8. In comparison with the much stronger correlation between Chl-a with SST in the East China Sea and the Eastern Coastal Water of the US, and between Chl-a with PAR in Amazon Estuary, there are no obvious correlations between Chl-a and environmental indices in the two enclosed seas. In addition, no distinct correlation between Chl-a and SWS is observed in all the five locations.

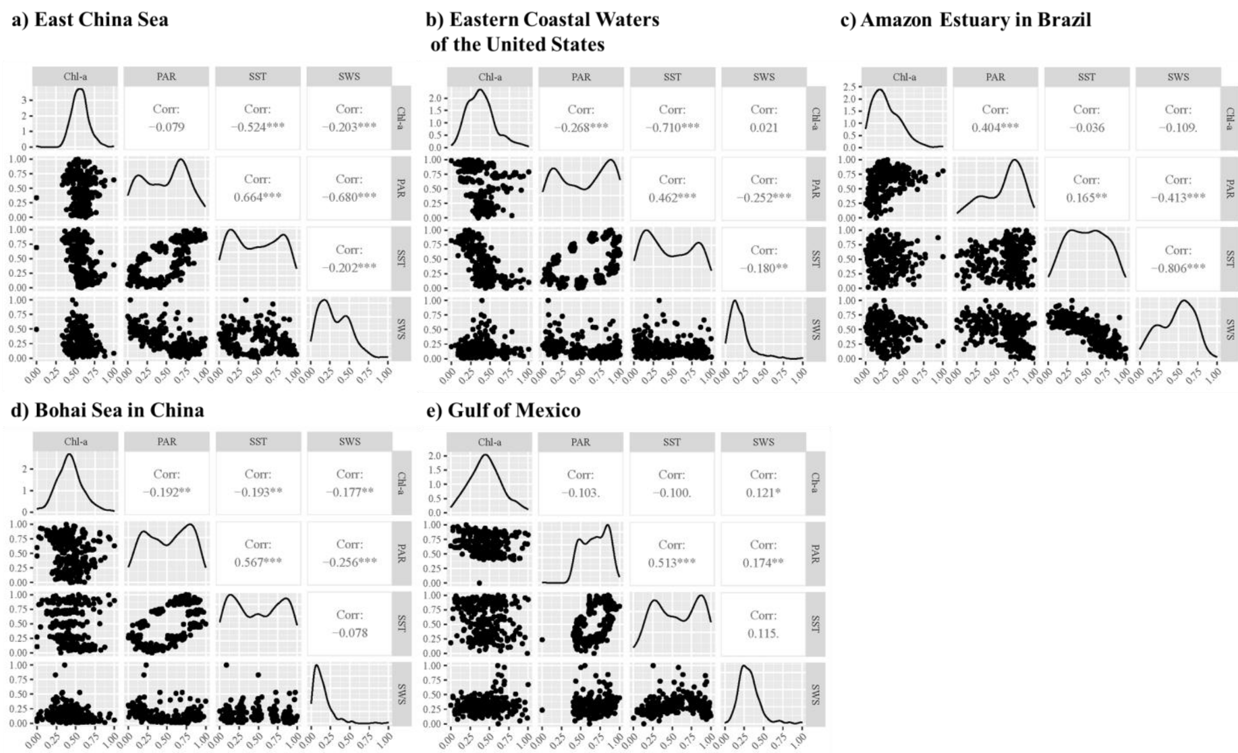

Figure 8. Spatial correlation matrices of Chl-a with environmental factors (SST, PAR, SWS) across five marginal sea areas: correlation coefficients (r) with significance levels (*p < 0.05, **p < 0.01, ***p < 0.001) labelled, and distribution histograms for each variable

Among the three open seas, trends and degrees of correlations between Chl-a with SST, PAR, and SWS differed markedly. All the three open seas show negative correlations between Chl-a and SST. Specifically, Amazon Estuary demonstrates a weaker negative correlation between Chl-a and SST than the East China Sea and the Eastern Coastal Waters of the US, but exhibits a significant positive correlation between Chl-a and PAR. A stronger negative correlation between Chl-a and SWS is observed in the East China Sea, while both Eastern Coastal Waters of US and Amazon Estuary exhibit insignificant correlations. In contrast, in the two enclosed seas (Gulf of Mexico and Bohai Sea), Chl-a showed weak or negligible correlation with and SST, SWS and PAR in both the Gulf of Mexico and the Bohai Sea indicate a relatively weak influence from environment on Chl-a in the enclosed sea areas.

Notably, varying degrees of inter correlations among the three indices are indicated in the five sea areas. Distinct positive correlation between SST and PAR are indicated except in Amazon Estuary. Besides, various degree of negative correlation between PAR and SWS are indicated with correlation coefficient of the East China Sea >Amazon Estuary > the East Coastal Waters of the U.S. ≈ the Bohai Sea, whereas the Gulf of Mexico demonstrate weak positive correlation. As for the correlation between SST and SWS, strong negative correlation is only observed in Amazon Estuary, while the other four sea areas exhibit weak negative/negative correlation.

Table 6. PCA analysis for the five study locations, for the three environment indices

Sea area	Influencing factors	Principle Component 1	Principle Component 2
The East China Sea	PAR	0.26	0.079
	SST	0.26	0.139
	SWS	0.111	0.141
The Eastern Coastal Waters of the US	PAR	0.29	0.147
	SST	0.245	0.175
	SWS	0.042	0.011
Amazon Estuary	PAR	0.135	0.202
	SST	0.22	0.103
	SWS	0.208	0.022
The Bohai Sea	PAR	0.234	0.146
	SST	0.286	0.123
	SWS	0.023	0.038
The Gulf of Mexico	PAR	0.108	0.078
	SST	0.276	0.04
	SWS	0.024	0.113

To clarify the key factors dominating Chl-a concentration, PCA was conducted for each study area. As shown in Tab. 6, SST had a relatively high loading on the first principal component across all five sea areas. In the east China Sea, PAR had a loading comparable to SST, while in the Eastern Coastal Waters of the US, PAR showed a higher loading than SST. In the Bohai Sea, PAR had a slightly lower loading than SST, and it was much lower than SST in the Gulf of Mexico and Amazon Estuary. These results suggest that seasonal SST variation in the Eastern Coastal Waters of the US, and the Bohai Sea is closely associated with seasonal PAR variation. In contrast, in Amazon Estuary, sustained solar irradiance near the equator may weaken the coupling between SST and PAR, making SST more susceptible to oceanic water intrusion and hydrological processes. In the Gulf of Mexico, SST variation may be strongly influenced by ocean circulation, including the Gulf Stream, explaining the lower PAR loading on the first principal component. SWS showed larger loadings on the first principal component in the three open sea areas than in the Bohai Sea and the Gulf of Mexico, possibly reflecting wind-driven vertical mixing and nutrient input from deeper waters.

In general, the loading on the first principle component likely relates to seasonal variation of SST, PAR, and SWS. The enclosed sea area of the Bohai Sea and the Gulf of Mexico are more susceptible to impact from seasonal SST variation, and have less impact from SWS. For the open sea areas of Eastern Coastal Waters of US and the East China Sea, both the seasonal variation of SST and PAR are more important in enhancing phytoplankton biomass. In contrast, for Amazon Estuary of Brazil, which is located at the equator, the guarantee of solar irradiance makes SST independent from PAR, and PAR is less significantly impacting Chl-a than SST and SWS.

4.2 Key factors impacting Chl-a concentration

The regulation of Chl-a concentrations across the five locations emerges from a complex interplay between physical forcing and biogeochemical cycles. The dominant driver basically shifts from climatic factors in open oceans to anthropogenic nutrients in enclosed seas.

4.2.1 Natural environmental factors

SST, PAR, and SWS exhibit regional regulations on Chl-a concentrations. For the open seas, the distinct negative correlations between SST and Chl-a in the East China Sea and East Coast, U.S. indicate the suppressive effect of Chl-a by SST increase in the context of global warming, aligning with the paradigm that warming intensifies stratification, thereby limiting the vertical flux of nutrients to the euphotic zone (Behrenfeld et al., 2006; Gong et al., 2003). In this context, the influence exerted by seasonally varying SST needs to be cautious. Whereas Amazon Estuary presented a notable anomaly with an insignificant SST-Chl-a correlation. This decoupling supports the hypothesis that SST in this region are primarily a passive tracer of low-salinity plume intrusions rather than a direct biological driver. The formation of a near-surface barrier layer, which inhibits mixing and elevates SST independently of atmospheric heating (Balaguru et al., 2012; Coles et al.,2013; Ferry and Reverdin, 2004; Grodsky et al., 2012). It explains the reason why PAR, rather than SST, governs local phytoplankton dynamics here (Gomes et al., 2018; Foltz et al., 2009). Similar to SST, the effect of PAR on Chl-a is also diverse. High turbidity may reduce the solar radiation available to phytoplankton and lead to regionally low biomass, such as in Hangzhou Bay, the northern Changjiang Estuary of the East China Sea. In addition, open sea areas experience greater sensitivity to SWS compared to the enclosed seas. SWS is closely related to current and upwelling activity, which have profound impacts on the Chl-a concentration. Several ocean circulation-influenced regions exhibit poor stability in terms of their Chl-a concentration due to upwelling of deeper seawater with suitable SST, salinity, and nutrients for phytoplankton growth (as shown in Fig. 6 and Fig. 7).

Different from the open seas, the sensitivity to SST, SWS and PAR is significantly different in enclosed systems. The very weak correlations between Chl-a and SST, PAR, SWS, indicating these natural environment factors play insignificant impact on the long term change of Chl-a. However, the stability of the regions where large ocean currents interact with seawater (such as the sea area near the Bohai Strait and in the Gulf Stream active area) is consistently low throughout the year (as shown in Fig. 6 and Fig.7), suggesting that the oceanic currents are an important factor that can not be ignored in enclosed seas, and it is closely intertwined with marine environmental indices such as SST and SWS. Besides, enclosed sea areas present a more complex seasonal pattern of Chl-a distribution. Particularly, the Bohai Sea exhibited complex seasonal patterns where physical factors were often overridden by local retention and biological consumption, such as zooplankton grazing, leading to late-summer Chl-a minima (Duan et al., 2020; Ministry of Water Resources, PRC, 2021).

4.2.2 Warming effects on Chl-a under regional thermal variability

To isolate the impact of global warming from seasonal cycles, relationships between SST and Chl-a during periods of SST rising versus stable are compared at the five locations (Fig. 9). Compared to the enclosed sea areas, the open seas are more significantly affected by temperature variations, the proportion of correlations during rising and stable SST periods exhibits distinct opposite distribution pattern. For example, during SST rise, the area with negative correlations increases significantly in the East China Sea, reaching 71.92% of the total, and similarly in Eastern Coastal Waters of the US at 68.15%. The stronger negative correlations mainly distributed in the areas with the saline intrusion. Notably, nearshore areas and estuarine plume-influenced regions like the Changjiang Estuary (Fig. 9a the East China Sea) consistently show positive Chl-a-SST correlations regardless of temperature changes. This consistent shift towards negative correlations across most regions during warming periods, particularly in offshore areas, coinciding with the intrusion of heated, oligotrophic saline waters (e.g., Kuroshio and Gulf Stream intrusions) (Tan and Cai, 2018; Walsh et al., 2005). This mirrors the "ocean desert expansion" observed in subtropical gyres globally (Polovina et al., 2008). In contrast, nearshore regions, regardless of basin type, maintained positive Chl-a-SST correlations. This persistence is attributed to the synergistic effect of rising temperatures amplifying the bioavailability of terrestrial nutrient inputs (Glibert et al., 2014).

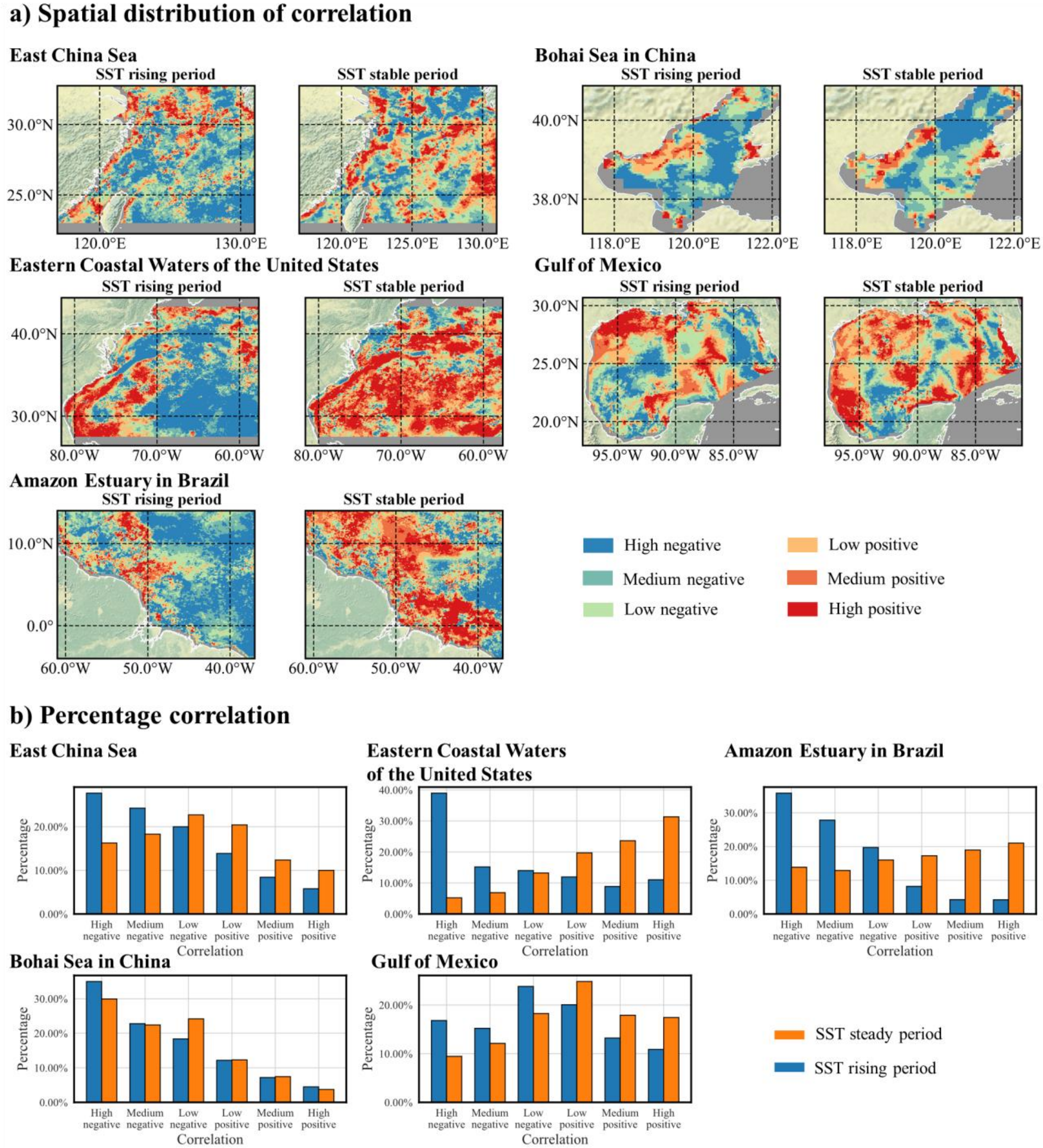

Figure 9. Spatial distribution and correlation proportion between SST- Chl-a in five marginal seas, 1998–2020. a) Spatial patterns of Pearson correlation coefficients in SST rising and stable stages. Color scale: blue = strong negative correlation (-1~-0.7, Chl-a declines with rising SST); green = moderate negative correlation (-0.7~-0.4); light green = weak negative correlation (-0.4~0); light orange = weak positive correlation (0~0.4); orange = moderate positive correlation (0.4~0.7); red = strong positive correlation (0.7~1.0, Chl-a rises with increasing SST); b) Proportional distribution of correlation magnitudes in different sea regions during SST rising (blue bars) and stable periods (orange bars).

Enclosed seas exhibited a similar dichotomy: 1) the central basins of the Bohai Sea and the Gulf of Mexico showed strengthened negative correlations of Chl-a-SST with warming, suggesting a link between temperature increases and lower phytoplankton biomass in these regions, which may result from stratification-induced nutrient limitation. 2) Specific regions such as (e.g., Mississippi and Luanhe River mouths, and Liaodong Bay) retained positive coupling due to continuous nutrient fertilization (Rabalais et al., 2007; Duan et al., 2020). This pattern may be estuarine plume influence, providing nutrients and enhancing Chl-a in some areas despite the overall negative correlation trend. Nevertheless, while these patterns highlight strong associations, correlation does not imply direct causation due to the influence of confounding physical and biological factors.

It is important to recognize that substantial sub-regional heterogeneity exists within the broad definitions of open and enclosed seas when generalizing the response of Chl-a to warming. For instance, the negative Chl-a-SST correlations observed in the open East China Sea are not uniform; they are modulated by localized physical processes such as the Changjiang Dilute Water plume and coastal upwelling, which introduce nutrient-rich waters and alter stratification. Similarly, the Gulf of Mexico exhibits complex spatial patterns where the influence of the Mississippi River plume contrasts with the oligotrophic conditions of the central basin. These findings highlight that while basin-scale geometry is important, intra-regional processes collectively shape the local magnitude and direction of Chl-a responses.

4.2.3 Anthropogenic nutrient inputs

Anthropogenic nutrient loading represents the primary driver of long-term Chl-a trends, particularly in enclosed seas and estuaries in open seas. Moreover, the environmental impacts of nutrients released by human activities may be further exacerbated by upwelling and other ocean currents, active in the coastal and estuarine zones, or in regions with limited water exchange. For example, in the East China Sea, high Chl-a concentrations primarily associated with the Changjiang River Plume and the presence of the Taiwan Warm Current, exhibit significant seasonal variation (Dai et al., 2022; Shi et al., 2023), particularly, a moderate increase in winter. Similarly, the East Coastal Water of the US demonstrates a gradient of decreasing Chl-a from nearshore to offshore and northwest to southeast, with seasonal peaks in spring and winter (Fig 4f), consistent with coastal bay nutrient dynamics. Amazon Estuary also reflects seasonal variability, with spring and summer high Chl-a areas expanding northeastward (Fig 4c), aligned with nutrient inflows from the Amazon River. In the Bohai Sea, high Chl-a concentrations are sustained in regions such as Laizhou Bay and the Liao River Estuary throughout the year, likely due to strong anthropogenic nutrient inputs under weaker hydrodynamic forces. In contrast, the Gulf of Mexico, though classified as enclosed sea, showcases high Chl-a zones mainly around the Mississippi River estuary and the Campeche Bay, where anthropogenic discharges and coastal upwelling play substantial roles (Martínez-López and Zavala-Hidalgo, 2009).

Situated within the rapidly developing economic belts of China, the Bohai Sea and the East China Sea receive massive nutrient fluxes. The high Chl-a concentrations in the Changjiang Estuary and Laizhou Bay are consistent with decades of coastal eutrophication due to industrial and agricultural runoff (Nixon, 1995; Seitzinger et al., 2010). Interestingly, the Gulf of Mexico exhibited the highest rate of Chl-a increase despite its strong connectivity with the Atlantic Ocean, suggesting that intensifying local anthropogenic pressures can counteract the mitigating effect of high water exchange (Turner et al., 2008).

A critical observation is the recent divergence in trends: while Amazon Estuary faces increasing nutrient influx due to rising fertilizer use in Brazil (Our World in Data, 2023), the Bohai Sea and the East China Sea have shown a deceleration or reversal of Chl-a increase post-2014. This aligns with the reported effectiveness of stringent environmental policies and pollution control measures implemented in China (Paerl et al., 2019; Li et al., 2024). In addition, the Gulf of Mexico shows the highest rate of Chl-a increase, the relationship with intensifying human activities despite its stronger connection to the Atlantic needs to pay attention.

It is noteworthy that Chl-a concentrations in the central basin of the Bohai Sea show a continued increase over time and remain relatively high. In addition, the outer Changjiang Estuary (under the impact of the Changjiang River Plume) shows significant increase in Chl-a, even though there is an obvious Chl-a decrease in the inner Changjiang Estuary (a similar phenomenon is observed in the plume of Amazon Estuary of Brazil, especially in the summer (Fig. 6)). This indicates that the long-term influence of land-sourced nutrient inputs is still expanding to more offshore regions. In these estuarine and nearshore systems, the trends in phytoplankton biomass correspond more strongly with the timeline of anthropogenic nutrient inputs than with the trends in SST rise.

Synthesizing these results reveals a hierarchical control mechanism across the five regions. First, in tropical, river-dominated systems of Amazon Estuary, freshwater plumes and light availability override thermal controls. Second, in temperate enclosed seas of Bohai, and the Gulf of Mexico, the system's response is a tug-of-war between terrestrial nutrient loading and warming-induced stratification through promoting or suppressing biomass growth. Third, in open seas of the East China Sea, the Eastern Coastal Waters of the US, large-scale physical processes including upwelling and saline intrusion dominate, although nearshore zones remain nutrient-sensitive. This regional heterogeneity underscores that while global climate models predict widespread declines in phytoplankton with warming, such predictions must be re-estimated by local anthropogenic activity strength and basin geometry, as highlighted in recent global syntheses of coastal ecosystems (Cloern et al., 2016; Kavanaugh et al., 2021).

5 Conclusions

In this study, a Chl-a time series dataset spanning 1998 to 2020 was created using monthly products from SeaWiFS/Chl-a and MODIS/Chl-a L3 products. The spatial and temporal variability of Chl-a in the Bohai Sea and the Gulf of Mexico, the East China Sea, Eastern Coastal Waters of US and Amazon Estuary was examined in relation to various degrees of anthropogenic disturbance and global warming, taking into account factors such as SWS, PAR, and other controls. The following conclusions were drawn from this research:

5.1 The opposing effects of SST on Chl-a

This study reveals two contrasting Chl-a responses to rising SST, which appear to be mediated by local environmental settings and nutrient availability. Generally, the widespread areas which show positive correlations between SST and Chl-a during stable SST periods (as shown in Fig. 9a the Gulf of Mexico and Fig.9a Amazon Estuary) are indicated to be related to seasonal SST variation. Additional anthropogenic nutrient inputs combined with the rising SST may stimulate phytoplankton proliferation, leading to increasing Chl-a along the coast in all five sea areas studied. Despite the control of pollutant emissions to the Bohai Sea and the East China Sea, a continuous increase in Chl-a in the central Bohai Sea and the Changjiang River Plume in the East China Sea are observed, although there is reduced Chl-a along coasts and estuaries as shown in Fig. 6 the East China Sea Annual and Fig. 6 the Bohai Sea Annual.

Meanwhile, a significant inhibitory effect of SST rise on Chl-a during typical warming periods is indicated. Negative correlations between Chl-a and SST are observed in most offshore areas which is consistent with saline sea water intrusion and influence of large current systems, such as the Taiwan Warm Current in the East China Sea, Gulf Stream along the Eastern Coastal Waters of the US, and the North Brazilian Current in Amazon Estuary. However, negative impacts from rising SST on nutrient supply are concealed by (land-derived) nutrient induced Chl-a enhancement especially in nearshore areas, and in the plumes of estuaries in the East China Sea and Amazon Estuary. It is important to note that in the Amazon Estuary, despite a significant increase of Chl-a in nearshore areas in 2020 compared to 2018, the overall Chl-a concentrations show a decreasing trend. This means that the falling trend in Chl-a in the offshore region owing to global warming effects may no longer be compensated for by additional anthropogenic nutrient inputs combining with rising SST in the coastal region and the estuary.

For the enclosed sea areas, the Gulf of Mexico exhibits a much lower eutrophication level than the Bohai Sea. Its larger spatial extent and stronger connectivity with the Atlantic Ocean, which is mediated by the Gulf Stream and Cuban Current, enhance water mass exchange and amplify warming impacts. Consequently, the Gulf of Mexico behaves more like an open sea system, displaying significant Chl-a declines during SST increases (Fig. 9a). These opposing responses underscore the need to better resolve sub-regional physical drivers (such as current and upwelling) that may synergize with warming to shape Chl-a trajectories.

5.2 Chl-a variation tendency under global warming and human response

The impact of global warming on Chl-a concentration is evident in all three open sea areas, namely Amazon Estuary, the East China Sea and the Eastern Coastal Waters of the US. Significant decreases in offshore Chl-a levels, strongly supporting a linkage to global warming rather than human activity, have been observed. If SSTs continue to rise and the contribution of riverine nutrients inputs decreases due to long-term pollution control measures, this ecological effect may extend to nearshore areas. Additionally, in the enclosed sea area of the Gulf of Mexico with medium eutrophic characteristics, the negative influence of global warming on Chl-a has also been identified. Rising SSTs and oceanic currents have led to a noticeable decline in Chl-a, particularly in areas where ocean currents enter the Gulf of Mexico. The negative correlation between SST and Chl-a in the central Gulf further supports the detrimental impact of global warming on Chl-a levels.

However, the impacts of rising SSTs under global warming in estuaries and along coastal waters are less pervasive than those from eutrophication. Eutrophication-induced phytoplankton blooms are expanding into offshore sea areas, even though Chl-a levels may decline along the coast due to controls on anthropogenic nutrient inputs. In highly eutrophic confined sea areas, such as the Bohai Sea, Chl-a levels appear to be less impacted by rising SSTs under global warming. Despite a decline in Chl-a concentrations in coastal waters of the Bohai Sea, the central basin still maintains high levels of Chl-a due to anthropogenic nutrient inputs, which currently masks the potential impact of global warming. However this lagging effect may be temporary and subject to future nonlinear threshold responses. In the highly eutrophic open sea of the East China Sea, although there has been a significant decline in the rate of Chl-a increase in estuaries and along the coast, Chl-a levels in the Changjiang River Plume continue to rise. This suggests that in sea areas with sufficient nutrients and suitable salinity, rising SST may further stimulate algal blooms. A similar phenomenon has been observed in the plume of Amazon Estuary, where the area of high Chl-a has expanded. Despite the widespread occurrence of decreasing Chl-a offshore, the continuous proliferation of phytoplankton in the plume compensates for the intrusion of warmer and oligotrophic pelagic waters.

This study contributes to our understanding of the ecological response of marine environments to both human activity and global warming. By continuously controlling the input of land-sourced nutrients, the frequency of algal blooms can be reduced, but high Chl-a levels may persist in estuaries and along the coast over the long term. From a broader perspective, nearshore areas will gradually experience greater impacts from global warming on nutrient supply. The study: (a) demonstrates the complex (and spatially variable) interactions between primary production, SST, and nutrient inputs and exchange under the dual pressures of changes in human activity and coastal development, and global warming; and (b) highlights the need for further research on the impacts of changing coastal and terrestrial nutrient inputs (including where these have been reduced due to environmental protection measures) on primary productivity in both enclosed and open sea areas. However, unresolved physical-biogeochemical feedbacks, such as warming-driven stratification and deoxygenation, limit mechanistic interpretations of these trends. Framing future research within the Global Carbon Project, GO_2NE, and marine ecosystem regime shift theory will help assess whether marginal seas are approaching ecological tipping points. Linking such insights to SDG 14 and the UN Ocean Decade is essential for adaptive coastal management and sustainable blue economy strategies under accelerating global change.

Author Contributions

X.Z. conceived the study and acquired funding and project administration and resource and supervision; N.Y. and X.Z. managed the data and method; N.Y. and S.M. performed the investigation and developed the software and validation; N.Y. and X.Z. analysed the data; N.Y. ,X.Z. and A.C. created the visualizations and wrote the original draft; and L.B., A.C., H.J., and R.L. reviewed and edited the manuscript.

Acknowledgments

This study was funded by Zhejiang Provincial Natural Science Foundation of China under Grant No. LD24D060001, and National Natural Science Foundation of China (U22B2012).

Open Research

The code used for data processing, analysis, and plotting in this study is available on GitHub: https://github.com/giseryn/Chlorophyll-a-Variation-Trends-in-Marginal-Seas. The code version used in this study is f7151f0e93458e0038aacb0a56c4537a4071f94d. The Chl-a and PAR data were obtained from NASA OceanColor: https://oceancolor.gsfc.nasa.gov/l3/order/ (last accessed: 25 May 2026). SST data were obtained from the NOAA AVHRR Pathfinder SST product: https://www.ncei.noaa.gov/products/avhrr-pathfinder-sst (last accessed: 25 May 2026). Ocean polygon data were obtained from Natural Earth: https://www.naturalearthdata.com/ (last accessed: 25 May 2026). Basin population density data were derived from the LandScan 2020 High Resolution Global Population Data Set: https://landscan.ornl.gov/ (last accessed: 25 May 2026).

References

Baker, K. G. and Geider, R. J.: Phytoplankton mortality in a changing thermal seascape, Global Change Biology, 27, 5253–5261, https://doi.org/10.1111/gcb.15772, 2021.

Behrenfeld, M. J., O’Malley, R. T., Boss, E. S., Westberry, T. K., Graff, J. R., Halsey, K. H., Milligan, A. J., Siegel, D. A., and Brown, M. B.: Revaluating ocean warming impacts on global phytoplankton, Nature Clim Change, 6, 323–330, https://doi.org/10.1038/nclimate2838, 2016.

Boyce, D. G., Lewis, M. R., and Worm, B.: Global phytoplankton decline over the past century, Nature, 466, 591–596, https://doi.org/10.1038/nature09268, 2010.

Cai, W., Santoso, A., Collins, M., Dewitte, B., Karamperidou, C., Kug, J.-S., Lengaigne, M., McPhaden, M. J., Stuecker, M. F., Taschetto, A. S., Timmermann, A., Wu, L., Yeh, S.-W., Wang, G., Ng, B., Jia, F., Yang, Y., Ying, J., Zheng, X.-T., Bayr, T., Brown, J. R., Capotondi, A., Cobb, K. M., Gan, B., Geng, T., Ham, Y.-G., Jin, F.-F., Jo, H.-S., Li, X., Lin, X., McGregor, S., Park, J.-H., Stein, K., Yang, K., Zhang, L., and Zhong, W.: Changing El Niño–Southern Oscillation in a warming climate, Nat Rev Earth Environ, 2, 628–644, https://doi.org/10.1038/s43017-021-00199-z, 2021.

Cai, W., Ng, B., Wang, G., Santoso, A., Wu, L., and Yang, K.: Increased ENSO sea surface temperature variability under four IPCC emission scenarios, Nat. Clim. Chang., 12, 228–231, https://doi.org/10.1038/s41558-022-01282-z, 2022.

Campos-Silva, J. V., Peres, C. A., Amaral, J. H. F., Sarmento, H., Forsberg, B., and Fonseca, C. R.: Fisheries management influences phytoplankton biomass of Amazonian floodplain lakes, Journal of Applied Ecology, 58, 731–743, https://doi.org/10.1111/1365-2664.13763, 2021.

Chen, C.-C., Shiah, F.-K., Gong, G.-C., and Chen, T.-Y.: Impact of upwelling on phytoplankton blooms and hypoxia along the Chinese coast in the East China Sea, Marine Pollution Bulletin, 167, 112288, https://doi.org/10.1016/j.marpolbul.2021.112288, 2021.

Chowdhury, K. M. A., Jiang, W., Liu, G., Ahmed, Md. K., and Akhter, S.: Dominant physical-biogeochemical drivers for the seasonal variations in the surface chlorophyll-a and subsurface chlorophyll-a maximum in the Bay of Bengal, Regional Studies in Marine Science, 48, 102022, https://doi.org/10.1016/j.rsma.2021.102022, 2021.

Cui, D., Liang, S., and Wang, D.: Observed and projected changes in global climate zones based on Köppen climate classification, WIREs Climate Change, 12, e701, https://doi.org/10.1002/wcc.701, 2021.

Dai, M., Su, J., Zhao, Y., Hofmann, E. E., Cao, Z., Cai, W.-J., Gan, J., Lacroix, F., Laruelle, G. G., Meng, F., Müller, J. D., Regnier, P. A. G., Wang, G., and Wang, Z.: Carbon Fluxes in the Coastal Ocean: Synthesis, Boundary Processes, and Future Trends, Annu. Rev. Earth Planet. Sci., 50, 593–626, https://doi.org/10.1146/annurev-earth-032320-090746, 2022.

Dai, Y., Yang, S., Zhao, D., Hu, C., Xu, W., Anderson, D. M., Li, Y., Song, X.-P., Boyce, D. G., Gibson, L., Zheng, C., and Feng, L.: Coastal phytoplankton blooms expand and intensify in the 21st century, Nature, 615, 280–284, https://doi.org/10.1038/s41586-023-05760-y, 2023.

Damien, P., Sheinbaum, J., Pasqueron de Fommervault, O., Jouanno, J., Linacre, L., and Duteil, O.: Do Loop Current eddies stimulate productivity in the Gulf of Mexico?, Biogeosciences, 18, 4281–4303, https://doi.org/10.5194/bg-18-4281-2021, 2021.

Dobson, J. E., Bright, E. A., Coleman, P. R., Durfee, R. C., and Worley, B. A.: LandScan: a global population database for estimating populations at risk, Photogrammetric engineering and remote sensing, 66, 849–857, 2000.

Duan, H., Wang, C., Liu, Z., Wang, H., Wu, X., and Xu, J.: Summer wind gusts modulate transport through a narrow strait, Bohai, China, Estuarine, Coastal and Shelf Science, 233, 106526, https://doi.org/10.1016/j.ecss.2019.106526, 2020.

Favareto, L., Brotas, V., Rudorff, N., Zacarias, N., Tracana, A., Lamas, L., Nascimento, Â., Ferreira, A., Gomes, M., Borges, C., Palma, C., and Brito, A. C.: Response of phytoplankton to coastal upwelling: The importance of temporal and spatial scales, Limnology and Oceanography, 68, 1376–1387, https://doi.org/10.1002/lno.12353, 2023.

Field, C. B., Behrenfeld, M. J., Randerson, J. T., and Falkowski, P.: Primary production of the biosphere: integrating terrestrial and oceanic components, Science, 281, 237–240, https://doi.org/10.1126/science.281.5374.237, 1998.

Frau, D., Gutierrez, M. F., Molina, F. R., and de Mello, F. T.: Drivers assessment of zooplankton grazing on phytoplankton under different scenarios of fish predation and turbidity in an in situ mesocosm experiment, Hydrobiologia, 848, 485–498, https://doi.org/10.1007/s10750-020-04456-y, 2021.

Friedlingstein, P., O'Sullivan, M., Jones, M. W., Andrew, R. M., Gregor, L., Hauck, J., Le Quéré, C., Luijkx, I. T., Olsen, A., Peters, G. P., Peters, W., Pongratz, J., Schwingshackl, C., Sitch, S., Canadell, J. G., Ciais, P., Jackson, R. B., Alin, S. R., Alkama, R., Arneth, A., Arora, V. K., Bates, N. R., Becker, M., Bellouin, N., Bittig, H. C., Bopp, L., Chevallier, F., Chini, L. P., Cronin, M., Evans, W., Falk, S., Feely, R. A., Gasser, T., Gehlen, M., Gkritzalis, T., Gloege, L., Grassi, G., Gruber, N., Gürses, Ö., Harris, I., Hefner, M., Houghton, R. A., Hurtt, G. C., Iida, Y., Ilyina, T., Jain, A. K., Jersild, A., Kadono, K., Kato, E., Kennedy, D., Klein Goldewijk, K., Knauer, J., Korsbakken, J. I., Landschützer, P., Lefèvre, N., Lindsay, K., Liu, J., Liu, Z., Marland, G., Mayot, N., McGrath, M. J., Metzl, N., Monacci, N. M., Munro, D. R., Nakaoka, S.-I., Niwa, Y., O'Brien, K., Ono, T., Palmer, P. I., Pan, N., Pierrot, D., Pocock, K., Poulter, B., Resplandy, L., Robertson, E., Rödenbeck, C., Rodriguez, C., Rosan, T. M., Schwinger, J., Séférian, R., Shutler, J. D., Skjelvan, I., Steinhoff, T., Sun, Q., Sutton, A. J., Sweeney, C., Takao, S., Tanhua, T., Tans, P. P., Tian, X., Tian, H., Tilbrook, B., Tsujino, H., Tubiello, F., van der Werf, G. R., Walker, A. P., Wanninkhof, R., Whitehead, C., Willstrand Wranne, A., et al.: Global Carbon Budget 2022, Earth System Science Data, 14, 4811–4900, https://doi.org/10.5194/essd-14-4811-2022, 2022.

Fu, Z., Hu, L., Chen, Z., Zhang, F., Shi, Z., Hu, B., Du, Z., and Liu, R.: Estimating spatial and temporal variation in ocean surface pCO2 in the Gulf of Mexico using remote sensing and machine learning techniques, Science of The Total Environment, 745, 140965, https://doi.org/10.1016/j.scitotenv.2020.140965, 2020.

Gregg, W. W. and Rousseaux, C. S.: Decadal trends in global pelagic ocean chlorophyll: A new assessment integrating multiple satellites, in situ data, and models, Journal of Geophysical Research: Oceans, 119, 5921–5933, https://doi.org/10.1002/2014JC010158, 2014.

Gregg, W. W., Casey, N. W., and McClain, C. R.: Recent trends in global ocean chlorophyll, Geophysical Research Letters, 32, https://doi.org/10.1029/2004GL021808, 2005.

Hallegraeff, G. M., Anderson, D. M., Belin, C., Bottein, M.-Y. D., Bresnan, E., Chinain, M., Enevoldsen, H., Iwataki, M., Karlson, B., McKenzie, C. H., Sunesen, I., Pitcher, G. C., Provoost, P., Richardson, A., Schweibold, L., Tester, P. A., Trainer, V. L., Yñiguez, A. T., and Zingone, A.: Perceived global increase in algal blooms is attributable to intensified monitoring and emerging bloom impacts, Commun Earth Environ, 2, 1–10, https://doi.org/10.1038/s43247-021-00178-8, 2021.

Hong, Z., Long, D., Li, X., Wang, Y., Zhang, J., Hamouda, M. A., and Mohamed, M. M.: A global daily gap-filled chlorophyll-*a* dataset in open oceans during 2001–2021 from multisource information using convolutional neural networks, Earth System Science Data, 15, 5281–5300, https://doi.org/10.5194/essd-15-5281-2023, 2023.

Hou, Z., Li, J., Diao, Y., Zhang, Y., Zhong, Q., Feng, J., and Qi, X.: Asymmetric influences of ENSO phases on the predictability of North Pacific sea surface temperature, Geophysical Research Letters, 51, e2023GL108091, 2024.

IPCC: Climate Change 2021: The Physical Science Basis. Contribution of Working Group I to the Sixth Assessment Report of the Intergovernmental Panel on Climate Change, Cambridge University Press, Cambridge, United Kingdom and New York, NY, USA, https://doi.org/10.1017/9781009157896, 2021.

Jickells, T. D.: Nutrient Biogeochemistry of the Coastal Zone, Science, 281, 217–222, https://doi.org/10.1126/science.281.5374.217, 1998.

Jin, D., Hoagland, P., and Buesseler, K. O.: The value of scientific research on the ocean's biological carbon pump, Science of The Total Environment, 749, 141357, https://doi.org/10.1016/j.scitotenv.2020.141357, 2020.

Ju, X., Ma, C., Yao, Z., and Bao, X.: Case analysis of water exchange between the Bohai and Yellow Seas in response to high winds in winter, J. Ocean. Limnol., 38, 30–41, https://doi.org/10.1007/s00343-019-9100-2, 2020.

Kaiser, J., Abel, S., Arz, H. W., Cundy, A. B., Dellwig, O., Gaca, P., Gerdts, G., Hajdas, I., Labrenz, M., Milton, J. A., Moros, M., Primpke, S., Roberts, S. L., Rose, N. L., Turner, S. D., Voss, M., and Ivar do Sul, J. A.: The East Gotland Basin (Baltic Sea) as a candidate Global boundary Stratotype Section and Point for the Anthropocene series, The Anthropocene Review, 10, 25–48, https://doi.org/10.1177/20530196221132709, 2023.

Kong, C. E., Yoo, S., and Jang, C. J.: East China Sea ecosystem under multiple stressors: Heterogeneous responses in the sea surface chlorophyll-a, Deep Sea Research Part I: Oceanographic Research Papers, 151, 103078, https://doi.org/10.1016/j.dsr.2019.103078, 2019.

Lebakula, V., Sims, K., Reith, A., Rose, A., McKee, J., Coleman, P., Kaufman, J., Urban, M., Jochem, C., Whitlock, C., Ogden, M., Pyle, J., Roddy, D., Epting, J., and Bright, E.: LandScan Global 30 Arcsecond Annual Global Gridded Population Datasets from 2000 to 2022, Sci Data, 12, 495, https://doi.org/10.1038/s41597-025-04817-z, 2025.

Lee, K. H., Jeong, H. J., Lee, K., Franks, P. J. S., Seong, K. A., Lee, S. Y., Lee, M. J., Hyeon Jang, S., Potvin, E., Suk Lim, A., Yoon, E. Y., Yoo, Y. D., Kang, N. S., and Kim, K. Y.: Effects of warming and eutrophication on coastal phytoplankton production, Harmful Algae, 81, 106–118, https://doi.org/10.1016/j.hal.2018.11.017, 2019.

Letscher, R. T., Moore, J. K., Martiny, A. C., and Lomas, M. W.: Pico-phytoplankton contribute half of global marine carbon export, https://doi.org/10.22541/essoar.167768119.97557585/v1, 2023.

Lloyd, C. T., Chamberlain, H., Kerr, D., Yetman, G., Pistolesi, L., Stevens, F. R., Gaughan, A. E., Nieves, J. J., Hornby, G., MacManus, K., Sinha, P., Bondarenko, M., Sorichetta, A., and Tatem, A. J.: Global spatio-temporally harmonised datasets for producing high-resolution gridded population distribution datasets, Big Earth Data, 3, 108–139, https://doi.org/10.1080/20964471.2019.1625151, 2019.

Ma, J. and Smith, W. O. J.: Primary Productivity in the Mid-Atlantic Bight: Is the Shelf Break a Location of Enhanced Productivity?, Front. Mar. Sci., 9, https://doi.org/10.3389/fmars.2022.824303, 2022.

Maćkiewicz, A. and Ratajczak, W.: Principal components analysis (PCA), Computers & Geosciences, 19, 303–342, https://doi.org/10.1016/0098-3004(93)90090-R, 1993.

Mao, Z., Gu, X., Cao, Y., Zhang, M., Zeng, Q., Chen, H., Shen, R., and Jeppesen, E.: The Role of Top-Down and Bottom-Up Control for Phytoplankton in a Subtropical Shallow Eutrophic Lake: Evidence Based on Long-Term Monitoring and Modeling, Ecosystems, 23, 1449–1463, https://doi.org/10.1007/s10021-020-00480-0, 2020.

Marrari, M., Piola, A. R., Valla, D., and Wilding, J. G.: Trends and variability in extended ocean color time series in the main reproductive area of the Argentine hake, Merluccius hubbsi (Southwestern Atlantic Ocean), Remote Sensing of Environment, 177, 1–12, https://doi.org/10.1016/j.rse.2016.02.011, 2016.

Martinez, E., Gorgues, T., Lengaigne, M., Fontana, C., Sauzède, R., Menkes, C., Uitz, J., Di Lorenzo, E., and Fablet, R.: Reconstructing Global Chlorophyll-a Variations Using a Non-linear Statistical Approach, Frontiers in Marine Science, 7, 2020.

Martínez-López, B. and Zavala-Hidalgo, J.: Seasonal and interannual variability of cross-shelf transports of chlorophyll in the Gulf of Mexico, Journal of Marine Systems, 77, 1–20, https://doi.org/10.1016/j.jmarsys.2008.10.002, 2009.

Mears, C. A., Scott, J., Wentz, F. J., Ricciardulli, L., Leidner, S. M., Hoffman, R., and Atlas, R.: A Near-Real-Time Version of the Cross-Calibrated Multiplatform (CCMP) Ocean Surface Wind Velocity Data Set, Journal of Geophysical Research: Oceans, 124, 6997–7010, https://doi.org/10.1029/2019JC015367, 2019.

Ministry of Ecology and Environment, PRC: China marine environmental quality bulletin, 2001.

Ministry of Ecology and Environment, PRC: Bulletin of Marine Ecology and Environment Status of China in 2020, 2021.

Ministry of Water Resources, PRC: Bulletin of Chinese river sediment (2020) The Ministry of Water Resources of the People's Republic of China, 2021.

Mizuta, D. D. and Wikfors, G. H.: Can offshore HABs hinder the development of offshore mussel aquaculture in the northeast United States?, Ocean & Coastal Management, 183, 105022, https://doi.org/10.1016/j.ocecoaman.2019.105022, 2020.

Moradi, M. and Moradi, N.: Correlation between concentrations of chlorophyll-a and satellite derived climatic factors in the Persian Gulf, Marine Pollution Bulletin, 161, 111728, https://doi.org/10.1016/j.marpolbul.2020.111728, 2020.

Mudelsee, M.: Trend analysis of climate time series: A review of methods, Earth-Science Reviews, 190, 310–322, https://doi.org/10.1016/j.earscirev.2018.12.005, 2019.

Pi, X., Zhao, S., Wang, W., Liu, D., Xu, C., Han, G., Kuang, T., Sui, S.-F., and Shen, J.-R.: The pigment-protein network of a diatom photosystem II–light-harvesting antenna supercomplex, Science, 365, eaax4406, 2019.

Pisano, A., Buongiorno Nardelli, B., Tronconi, C., and Santoleri, R.: The new Mediterranean optimally interpolated pathfinder AVHRR SST Dataset (1982–2012), Remote Sensing of Environment, 176, 107–116, https://doi.org/10.1016/j.rse.2016.01.019, 2016.

Reid, P. C., Battle, E. J. V., Batten, S. D., and Brander, K. M.: Impacts of fisheries on plankton community structure, ICES Journal of Marine Science, 57, 495–502, https://doi.org/10.1006/jmsc.2000.0740, 2000.

Shi, Y., Zhang, M., Xu, X., He, M., Liu, Y., Du, J., Zhao, M., Wei, Q., Liu, D., and Gao, J.: Ecological effects of offshore transport in the shelf sea and its response to climate warming, Global and Planetary Change, 229, 104240, https://doi.org/10.1016/j.gloplacha.2023.104240, 2023.

Siemer, J. P., Machín, F., González-Vega, A., Arrieta, J. M., Gutiérrez-Guerra, M. A., Pérez-Hernández, M. D., Vélez-Belchí, P., Hernández-Guerra, A., and Fraile-Nuez, E.: Recent Trends in SST, Chl-a, Productivity and Wind Stress in Upwelling and Open Ocean Areas in the Upper Eastern North Atlantic Subtropical Gyre, Journal of Geophysical Research: Oceans, 126, e2021JC017268, https://doi.org/10.1029/2021JC017268, 2021.

Subramaniam, A., Yager, P. L., Carpenter, E. J., Mahaffey, C., Björkman, K., Cooley, S., Kustka, A. B., Montoya, J. P., Sañudo-Wilhelmy, S. A., Shipe, R., and Capone, D. G.: Amazon River enhances diazotrophy and carbon sequestration in the tropical North Atlantic Ocean, Proceedings of the National Academy of Sciences, 105, 10460–10465, https://doi.org/10.1073/pnas.0710279105, 2008.

Wang, H., Fu, D., Liu, D., Xiao, X., He, X., and Liu, B.: Analysis and Prediction of Significant Wave Height in the Beibu Gulf, South China Sea, Journal of Geophysical Research: Oceans, 126, e2020JC017144, https://doi.org/10.1029/2020JC017144, 2021.

Wang, X.: Advance in the Inter-annual Variability of Vegetation and Its Relation to Climate Based on Remote Sensing, Journal of remote sensing, 421–431, https://doi.org/10.11834/jrs.20060363, 2006.

Wang, Y. and Xiu, P.: Typhoon footprints on ocean surface temperature and chlorophyll-*a* in the South China Sea, Science of The Total Environment, 840, 156686, https://doi.org/10.1016/j.scitotenv.2022.156686, 2022.

Xi, H., Losa, S. N., Mangin, A., Garnesson, P., Bretagnon, M., Demaria, J., Soppa, M. A., Hembise Fanton d'Andon, O., and Bracher, A.: Global Chlorophyll a Concentrations of Phytoplankton Functional Types With Detailed Uncertainty Assessment Using Multisensor Ocean Color and Sea Surface Temperature Satellite Products, Journal of Geophysical Research: Oceans, 126, e2020JC017127, https://doi.org/10.1029/2020JC017127, 2021.

Yingling, N., Kelly, T. B., Shropshire, T. A., Landry, M. R., Selph, K. E., Knapp, A. N., Kranz, S. A., and Stukel, M. R.: Taxon-specific phytoplankton growth, nutrient utilization and light limitation in the oligotrophic Gulf of Mexico, Journal of Plankton Research, 44, 656–676, https://doi.org/10.1093/plankt/fbab028, 2022.

Zhang, C., Hu, C., Shang, S., Müller-Karger, F. E., Li, Y., Dai, M., Huang, B., Ning, X., and Hong, H.: Bridging between SeaWiFS and MODIS for continuity of chlorophyll-a concentration assessments off Southeastern China, Remote Sensing of Environment, 102, 250–263, https://doi.org/10.1016/j.rse.2006.02.015, 2006.

Zhou, Z.-X., Yu, R.-C., and Zhou, M.-J.: Evolution of harmful algal blooms in the East China Sea under eutrophication and warming scenarios, Water Research, 221, 118807, https://doi.org/10.1016/j.watres.2022.118807, 2022.

Appendix

Appendix A：Chl-a concentration and PAR fitting equations obtained from SeaWiFS and MODIS satellites for each study area

Overlapping Chl-a data from MODIS and SeaWiFS during the T2 period were processed with linear regression equations for each month in various sea areas ($y = ax + b$, x, y are the Chl-a values of SeaWiFS and MODIS, respectively); and data with R2 below 0.5 were not corrected. When R2 was greater than 0.5, the equation derived from this linear regression was used to correct SeaWiFS\Chl-a. The regression results values for each sea area are listed bellow. The construction methods are shown as follows:

T1 period: corrected SeaWiFS\Chl-a values substitute for the original data of corresponding months ($\mathrm{Chl-a_{SWFcorr}}$). For months without correction, the original SeaWiFS\Chl-a ($\mathrm{Chl-a_{SWF}}$) are used.

T2 period: Chl-a values are calculated through averaging the data from MODIS ($\mathrm{Chl-a_{MOD}}$) and SeaWiFS($\mathrm{Chl-a_{SWFcorr}}/\mathrm{Chl-a_{SWF}}$).

$$\mathrm{Chl-a_{T2}} = (\mathrm{Chl-a_{SWF}} + \mathrm{Chl-a_{MOD}})/2$$

$$\mathrm{Chl-a_{T2}} = (\mathrm{Chl-a_{SWFCORR}} + \mathrm{Chl-a_{MOD}})/2$$

T3 period: only MODIS\Chl-a data are available, $\mathrm{Chl-a_{MOD}}$ are used directly.

Table A1. Monthly R^2 values of Chl-a fitting between SeaWiFS and MODIS for each study area.

	The Bohai Sea	The Gulf of Mexico	The East China Sea	The Eastern Coastal Waters of the US	Amazon Estuary
January	0.071	**0.229**	0.120	**0.046**	0.007
February	0.018	0.397	0.073	0.371	0.017
March	0.126	**0.967**	0.003	**0.220**	0.301
April	0.064	0.911	0.509	**0.898**	0.278
May	**0.251**	**0.941**	**0.305**	**0.096**	0.000
June	0.840	0.948	0.062	0.687	0.803
July	**0.070**	**0.003**	**0.245**	**0.131**	**0.410**
August	**0.842**	0.604	**0.547**	0.863	0.715

September	**0.149**	**0.141**	**0.590**	**0.214**	**0.435**
October	**0.000**	**0.001**	0.001	**0.003**	**0.012**
November	0.102	0.906	0.499	0.603	0.375
December	0.049	0.939	0.772	0.114	0.630

Table A2. Monthly R^2 values of PAR fitting between SeaWiFS and MODIS for each study area.

	The Bohai Sea	The Gulf of Mexico	The East China Sea	The Eastern Coastal Waters of the US	Amazon Estuary
January	0.826	**0.146**	0.954	**0.025**	0.655
February	0.814	0.992	0.988	0.938	0.983
March	0.625	**0.329**	0.841	**0.218**	0.985
April	0.721	0.710	0.921	**0.418**	0.847
May	**0.001**	**0.103**	**0.000**	**0.030**	0.817
June	0.964	0.826	0.889	0.837	0.603
July	**0.161**	**0.322**	**0.082**	**0.131**	**0.060**
August	**0.135**	0.513	**0.500**	0.919	0.802
September	**0.351**	**0.008**	**0.019**	**0.260**	**0.056**
October	**0.024**	**0.028**	0.655	**0.146**	**0.095**
November	0.969	0.971	0.951	0.507	0.673
December	0.585	0.987	0.695	0.859	0.978

Based on the threshold of $R^2 > 0.5$, the months requiring correction are summarized below.

Months that require correction Chl-a concentration in the East China Sea include April, August, September, and December.

$$y = 0.661x + 0.251$$

$$y = 0.571x + 0.233$$

$$y = 0.246x + 0.400$$

$$y = 0.439x + 0.323$$

Months that require correction Chl-a concentration in the Eastern Coastal Waters of US include April, August, November.

$$y = 0.672x + 0.145$$

$$y = 0.835x + 0.086$$

$$y = 1.007x + 0.008$$

Months that require correction Chl-a concentration in the Amazon Estuary include June, August, December.

$$y = 0.48x + 0.233$$

$$y = 0.519x + 0.198$$

$$y = 0.735x + 0.091$$

Months that require correction Chl-a concentration in the Bohai Sea include June, August, December .

$$y = 0.851x + 0.424$$

$$y = 1.052x + 0.154$$

$$y = 0.735x + 0.091$$

Months that require correction Chl-a concentration in the Gulf of Mexico include March, April, May, June, July, August, November, December.

$$y = 0.937x + 0.071$$

$$y = 0.902x + 0.090$$

$$y = 0.758x + 0.132$$

$$y = 0.614x + 0.192$$

$$y = -0.021x + 0.558$$

$$y = 0.366x + 0.328$$

$$y = 1.139x + 0.009$$

$$y = 1.061x + 0.033$$

Months that require correction PAR data in the East China Sea include January, February, March, April, June, August, October, November, December.

$$y = 0.7407x + 3.0500$$

$$y = 0.9062x + 1.2272$$

$$y = 0.6633x + 7.4084$$

$$y = 1.1265x \pm 4.7338$$

$$y = 0.9306x + 0.3926$$

$$y = 0.5859x + 15.0874$$

$$y = 0.5185x + 12.0817$$

$$y = 0.8109x + 2.7642$$

$$y = 0.4869x + 6.9225$$

Months that require correction PAR data in the Amazon Estuary include January, February, March, April, May, June, August, November, December.

$$y = 0.6712x + 9.4768$$
$$y = 1.1324x \pm 4.8767$$
$$y = 1.1223x \pm 4.8357$$
$$y = 0.9561x + 1.1267$$
$$y = 0.9114x + 2.4527$$
$$y = 0.6899x + 9.6201$$
$$y = 0.8800x + 4.0144$$
$$y = 0.5721x + 12.6073$$
$$y = 1.1020x \pm 3.2767$$

Months that require correction PAR data in the Bohai Sea include January, February, March, April, June, November, December.

$$y = 1.1750x \pm 1.8659$$
$$y = 1.2591x \pm 3.4065$$
$$y = 0.4278x + 8.6293$$
$$y = 0.6687x + 5.9476$$
$$y = 0.9130x + 1.2173$$
$$y = 0.8262x + 1.2522$$
$$y = 0.4056x + 4.1002$$

Months that require correction PAR data in the Gulf of Mexico include January, February, March, April, June, November, December.

$$y = 1.0927x \pm 2.2949$$
$$y = 0.9091x + 2.7284$$
$$y = 1.2825x \pm 10.5483$$
$$y = 0.3289x + 21.2346$$
$$y = 1.0825x \pm 1.7048$$
$$y = 1.1187x + -2.0893$$

Appendix B：Outlier Removal in Time Series Analysis

To reduce the influence of extreme values on the long-term time-series analysis, an outlier removal procedure was applied before calculating the pixel-level trend and coefficient of variation. For each pixel-level time series, a statistical threshold based on three times the standard deviation was used to identify anomalous values. The method assumes that data points lying far from the mean are relatively rare and may represent abnormal fluctuations.

The criterion for identifying outliers can be expressed as:

$$X_{outlier} \notin [\mu - 3\sigma, \mu + 3\sigma]$$

Where $X_{outlier}$ represents the outlier values, μ is the mean of the data, and σ is the standard deviation. Data points outside the range $[\mu - 3\sigma, \mu + 3\sigma]$ were flagged as outliers and excluded from further analysis.

After outlier removal, the filtered time series was used to calculate the linear trend and coefficient of variation for each pixel. This procedure reduced the potential influence of extreme values on the estimation of temporal trends and variability. In the implemented workflow, the outlier removal was performed once for each pixel-level time series before the final statistical calculations.

.

Appendix C：Slope Trend Analysis

The annual variation rate slope of Chl-a from 1998 to 2020 is calculated using the least squares method. This method determines the linear trend in the data by fitting a straight line through the time series, where the slope represents the average annual rate of change. The slope is calculated using the following formula:

$$\text{Slope} = \frac{n\sum_{i=1}^{n} (i \times Chla_i) - \sum_{i=1}^{n} i_{i=1}^{n} Chla_i}{n \times \sum_{i=1}^{n} i - \sum_{i=1}^{n} i}$$

This formula minimizes the residual errors between the observed Chl-a values and the values predicted by the fitted line, ensuring the most accurate representation of the trend. The slope obtained provides a quantitative measure of the rate of change in Chl-a concentration over the period. A positive slope indicates an increasing trend in Chl-a concentrations, while a negative slope signifies a decreasing trend.

Appendix D：Stability Analysis

The stability of a time series over time can be evaluated using C_v, which provides a standardized measure of the dispersion of the data relative to its mean. This is particularly useful for understanding the consistency of values in the time series across the observed period. The formula for C_v is expressed as:

$$C_v = \frac{1}{\bar{x}}\sqrt{\frac{\sum_{i=1}^{n} (x_i - \bar{x}^2)}{n-1}}$$

A lower C_v indicates greater stability in the time series, with less variation relative to the mean, while a higher C_v suggests more significant fluctuations over time.

Appendix E：Areas with increasing or decreasing trend of Chl-a from 1998 to 2020

Sea area	Season	Trend	Ratio of the total area	Sea area	Season	Trend	Ratio of the total area
The East China Sea	Spring	Decreasing	69.74%	The Bohai Sea	Spring	Decreasing	67.06%
		Increasing	30.26%			Increasing	32.94%
	Summer	Decreasing	76.24%		Summer	Decreasing	22.34%
		Increasing	23.76%			Increasing	77.66%
	Autumn	Decreasing	70.21%		Autumn	Decreasing	84.35%
		Increasing	29.79%			Increasing	15.65%
	Winter	Decreasing	78.44%		Winter	Decreasing	84.40%
		Increasing	21.56%			Increasing	15.60%
	Annual	Decreasing	73.89%		annual	Decreasing	66.21%
		Increasing	26.11%			Increasing	33.79%

Sea area	Season	Trend	Ratio of the total area	Sea area	Season	Trend	Ratio of the total area
The Eastern Coastal Waters of US	Spring	Decreasing	90.57%	The Gulf of Mexico	Spring	Decreasing	81.97%
		Increasing	9.42%			Increasing	17.96%
	Summer	Decreasing	91.85%		Summer	Decreasing	76.81%
		Increasing	8.06%			Increasing	23.11%
	Autumn	Decreasing	84.65%		Autumn	Decreasing	61.87%
		Increasing	15.34%			Increasing	38.01%
	Winter	Decreasing	78.97%		Winter	Decreasing	57.38%
		Increasing	21.02%			Increasing	42.54%
	Annual	Decreasing	93.47%		Annual	Decreasing	77.97%
		Increasing	6.53%			Increasing	21.94%

Sea area	Season	Trend	Ratio of the total area
Amazon Estuary	Spring	Decreasing	84.77%
		Increasing	15.23%
	Summer	Decreasing	80.51%
		Increasing	19.49%

Autumn	Decreasing	49.49%
	Increasing	50.51%
Winter	Decreasing	75.56%
	Increasing	24.43%
Annual	Decreasing	82.81%
	Increasing	17.19%

Appendix F：Annual and seasonal stability of Chl-a in the five location from 1998-2020

		The Bohai Sea	The Gulf of Mexico	The East China Sea	The Eastern Coastal Waters of the US	Amazon Estuary
	Level of Stability	Ratio of the Area	Ratio of the Area	Ratio of the Area	Ratio of the Area	Ratio of the Area
Annual	High	0.11%	0.00%	0.01%	0.01%	0.00%
	Medium to high	67.51%	0.42%	6.13%	2.91%	1.67%
	Medium	24.62%	8.42%	21.05%	41.54%	17.13%
	Medium to low	4.28%	36.98%	22.73%	33.43%	26.77%
	Low	3.47%	54.18%	50.08%	22.11%	54.43%
Spring	High	0.06%	0.00%	0.00%	0.00%	0.00%
	Medium to high	5.46%	0.47%	0.05%	0.03%	0.45%
	Medium	62.33%	1.50%	3.11%	1.61%	16.04%
	Medium to low	22.58%	6.03%	10.13%	13.86%	33.75%
	Low	9.57%	92.01%	86.71%	84.50%	49.76%
Summer	High	0.06%	0.00%	0.00%	0.00%	0.01%
	Medium to high	8.61%	0.00%	0.27%	0.15%	0.76%
	Medium	25.43%	0.25%	1.90%	3.21%	1.61%
	Medium to low	23.02%	1.17%	11.32%	7.24%	2.73%
	Low	42.87%	98.59%	86.51%	89.40%	94.89%
Autumn	High	0.00%	0.00%	0.00%	0.00%	0.00%
	Medium to high	35.17%	0.28%	1.73%	0.64%	2.72%
	Medium	52.14%	10.36%	4.12%	19.33%	20.54%
	Medium to low	6.50%	32.19%	9.66%	50.55%	20.27%
	Low	6.18%	57.17%	84.48%	29.47%	56.47%
Winter	High	0.02%	0.00%	0.04%	0.03%	0.00%
	Medium to high	28.44%	3.59%	7.19%	14.96%	0.67%
	Medium	57.77%	47.75%	11.15%	37.26%	22.07%
	Medium to low	7.12%	24.81%	29.39%	25.90%	47.55%
	Low	6.65%	23.84%	52.24%	21.84%	29.71%